Numerical tiling-based simulations of decoherence in multifield models of inflation

Johor D. Peñalba Quispitupa , 1, * Guillermo F. Quispe Peña , 2, † and José T. Gálvez Ghersi , 1 Facultad de Ciencias - Universidad Nacional de Ingeniería; Av. Tupac Amaru 210 - Rimac, Lima, Perú 2 Simon Fraser University, 8888 University Dr. W, Burnaby, BC V5A 1S6 3 Universidad de Ingenieria y Tecnologia; Jr. Medrano Silva 165 - Barranco 15063, Lima, Perú (Dated: November 24, 2025)

In previous work, we developed a method for computing two-point correlators by decomposing the mode degrees of freedom into fast and slow components. Building on this framework, we present a numerical implementation to study the evolution of primordial scalar perturbations under controlled state deformations induced by the simplest environment corrections from the Lindblad equation. Our approach generalizes to an arbitrary number of degrees of freedom and does not rely on the slow-roll approximation. The computational routine is numerically efficient and allows users to configure arbitrary sequences of decoherence events, with full control over their duration, shape, amplitude and effective wavelength range. The resulting outputs are compatible with nonlinear numerical codes, enabling studies of how decoherence effects propagate during reheating.

I. INTRODUCTION

At the perturbative level, the inflationary model has been remarkably successful since its inception [1–4]. It provides an effective mechanism by which quantum-mechanical fluctuations produce the primordial inhomogeneities consistent with the nearly isotropic and homogeneous state of the early universe shown in the Cosmic Microwave Background (CMB) [5–7]. In the years to come, the enhanced resolution of the next–generation CMB observations [8–11] will allow for more stringent constraints on inflation, as well as in the emergence of primordial non-Gaussianities and potential gravitational wave backgrounds from polarization maps free from the effects of intergalactic dust.

Modifications to the dynamics of the inflationary adiabatic or the isocurvature fields – through potential [12–15], field geometry [16] and kinetic deformations [17] – have motivated investigations into possible connections with dark matter, oscillon production, formation of primordial black holes and non-Gaussianities, while remaining consistent with observations. In addition to these approaches, the open-quantum systems framework has been proposed to incorporate the effect of environmental operators via non-unitary distortions of the vacuum state [18–22]. We conjecture that this formalism is sufficiently general to span a substantial portion of the configuration space of initial Gaussian states, thereby enabling controlled state manipulations akin to the implementation of a pumping protocol in quantum optics [23, 24]. Even though only a subset of these initial conditions leads to modifications of the primordial spectrum consistent with current observations, the entire set remains essential. Together, they offer a comprehensive set of scenarios that (a) enable efficient forecasting of primordial non-Gaussianities during inflation with minimal computational cost, and (b) supply well-defined initial conditions to study the nonlinear evolution of overdensities during reheating, and posteriorly during large structure formation [25, 26].

The primary objective of this paper is to demonstrate how the first modifications introduced by the open quantum systems framework – which naturally induces initial state deformations through decoherence and recoherence - can be consistently combined with the nonlinear background evolution driven by an arbitrary number of fields during inflation, avoiding the use of the so-called slow-roll approximations. Obtaining exact solutions from a nonlinear system of background equations becomes increasingly challenging as the number of fields grows. In addition to this, one needs to resolve fast oscillations – which are computationally expensive – to find the exact evolution of perturbation mode equations. Therefore, numerical solutions are necessary to compute dynamical observables consistent with the background expansion, such as the evolving two-point correlation functions of scalar fluctuations. To this end, we have developed a technique based on the separation of fast and slow degrees of freedom [27, 28]. This approach reduces the computational cost of solving exactly both the evolution of the nonlinear background equations and the perturbation field correlations deep inside the horizon - precisely where decoherence events modify the behavior of the mode solutions. Hence, this procedure offers a scalable framework for introducing features into two-point correlators compatible with any sufficiently smooth inflationary background evolution, while remaining feasible on consumer-grade computers.

Building on this separation method, we modify the evolution scheme to solve the simplest realization of the Lindblad equation presented in [18-22], and extend it to the multifield case. The numerical routines are designed to accommodate an arbitrary sequence of decoherence events (or "accidents") acting on different k-modes at different times, without impacting on computational performance.

^{*} jpenalbag@uni.pe

[†] gfq@sfu.ca

[‡] jgalvezg@utec.edu.pe

This sequence defines the time-dependent power spectrum of the environmental operators and determines the resulting deformed state of each mode. The duration, amplitude and range of wavelengths of these events can be tuned to generate distinctive features in the evolution of Gaussian states and in the resulting power spectrum of primordial curvature fluctuations.

The fast and slow decomposition scheme employed here can also be interpreted as a dynamical coloring transformation based on Cholesky decomposition. Such transformations can be applied to any set of unit-variance random variables to generate initial conditions for the inflationary fields, which can be subsequently evolved nonlinearly using reheating codes [29]. The computational routines developed for this study are publicly available in https://github.com/JohorD.

The remainder of this paper is organized as follows. In Section II, we review the open quantum system formalism in the context of inflationary models driven by a single scalar field. We also introduce the foundations of our fastslow scale separation scheme and compute the curvature power spectrum under the influence of multiple accidents introducing decoherence. In Section III, we extend our component separation method to incorporate decoherence effects in multifield inflation models. Our results demonstrate that it is possible to generate features in the power spectrum of primordial curvature fluctuations across any range of wavelengths. Using cross-correlations, we illustrate how decoherence propagates between isocurvature and isentropic degrees of freedom. In Appendix A, we show that our decomposition scheme can also be applied to other forms of coloring transformations beyond the Cholesky decomposition. In Appendix B, we construct three-dimensional field realizations from the outputs of our numerical routine. These field realizations can serve as initial conditions for simulations of the reheating phase. Finally, in Section IV, we discuss potential future applications of these routines and present our conclusions.

II. REVIEW OF THE OPEN QUANTUM SYSTEM FRAMEWORK

In this section, we present an overview of the background and the perturbative mode dynamics when inflation is driven by a single scalar field. Building on the open quantum system framework described in [18–21], the following subsections develop a numerical formalism to address the general case of an arbitrary configuration of state accidents – arising from decoherence and recoherence events – occurring at arbitrary instants of time and wavelengths. By tuning these configurations of decoherence events, we postulate that one can deform the initial states of a simple inflationary model to reproduce features in the primordial curvature spectrum typically associated to more intricate models.

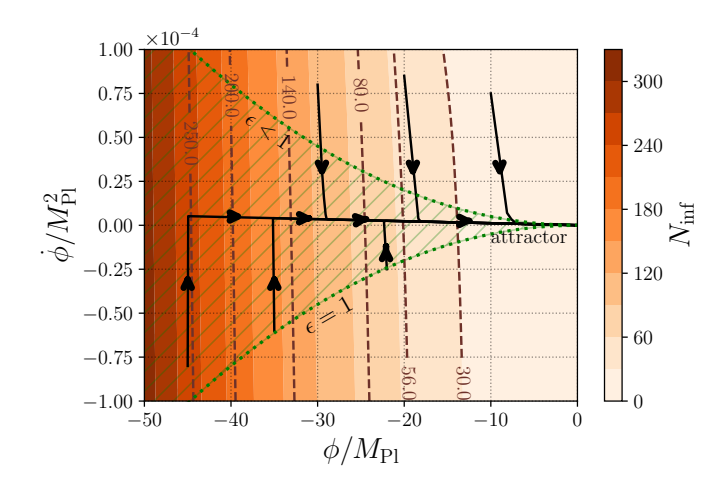


FIG. 1. Map of initial conditions for the potential $V(\phi) = \lambda \phi^4/4$ with $\lambda = 10^{-14}$. In this case, background trajectories converge to the attractor exponentially fast. The green dashed curves mark the boundaries where $\epsilon = 1$. Under the slow-roll approximation, the allowed region of background field configurations is restricted to the wedge shaded with green lines.

A. Single field inflation: dynamical setup for closed systems

We begin with a quick revision of the characteristic exponential expansion of the universe during cosmic inflation, which is driven by the dynamics of the inflaton field minimally coupled to gravity. Both geometry and field dynamics are governed by the following effective action

$$S = \int d^4x \sqrt{-g} \left[\frac{M_{\rm Pl}^2}{2} R - \frac{1}{2} g^{\mu\nu} \nabla_{\mu} \phi \nabla_{\nu} \phi - V(\phi) \right] , (1)$$

where $g \equiv \text{Det}(g_{\mu\nu})$, $M_{\text{Pl}} \equiv (8\pi G)^{-1/2}$ is the reduced Planck mass in units of $\hbar = c = 1$, and ϕ is the inflaton field. Throughout the paper, we use the signature (-,+,+,+) and the flat Friedmann-Lemaître-Robertson-Walker (FLRW) background metric as an invariant under gauge transformations. We choose the quartic potential $V(\phi) = \lambda \phi^4/4$ as a test case, but most of the dynamical features of the system do not depend on this choice.

The background inflaton dynamics is determined by the standard second-order equation of motion

$$\ddot{\phi} + 3H\dot{\phi} + V(\phi) = 0, \qquad (2)$$

where dots denote derivatives with respect to the cosmic time t. The evolution of the scale factor, in terms of the Hubble parameter $H \equiv \dot{a}/a$, follows from the two Friedmann equations

$$3M_{\rm Pl}^2 H^2 = \frac{\dot{\phi}^2}{2} + V(\phi),$$
 (3a)

$$-2M_{\rm Pl}^2 \dot{H} = \dot{\phi}^2 \,. \tag{3b}$$

In the slow-roll regime, inflation comes to an end when the parameter $\epsilon = \dot{\phi}^2/(2H^2)$ equals one. Figure 1 shows a map of initial conditions: each pixel represents a different initial choice of field values, and the color (indicated in the colorbar to the right) shows the corresponding number of e-folds of inflation, dubbed by $N_{\rm inf}$. The map is approximately symmetric about the axis $\phi=0$. In addition to this map, we display a few field trajectories that rapidly flow toward the inflationary attractor. The slow-roll approximation restricts the range of allowed field configurations to a wedge (hatched with thin green lines), bounded by the dotted green curves. While the restriction has no significant consequences for standard slow-roll models, it may preclude interesting field dynamics in scenarios where potential instabilities arise [30, 31].

In the case of gauge-invariant scalar perturbations (ζ), these arise from expanding the action in (1) up to second order in the $\delta\phi = 0$ gauge

$$S_2 = \frac{1}{2} \int d\tau \ d^3 \mathbf{x} \left(\frac{\phi'^2}{2H^2} \right) \left[\zeta'^2 - (\nabla^i \zeta)(\nabla_i \zeta) \right] , \quad (4)$$

where τ is the conformal time and primes denote derivatives with respect to it. Latin indices are reserved for cartesian coordinates, and are raised and lowered by the Kronecker delta. To introduce canonical normalization, Mukhanov-Sasaki variables are defined as $v=\phi'\zeta/H$, which enable us to rewrite the action as

$$S_2 = \frac{1}{2} \int d\tau \ d^3 \mathbf{x} \left[v'^2 - (\nabla_i v)(\nabla^i v) - \frac{z''}{z} v^2 \right], \quad (5)$$

where $z \equiv (\sqrt{2}M_{\rm Pl}H)^{-1}\phi'$. The corresponding Hamiltonian can be found by performing a Legendre transformation of the action

$$H_{\text{sys}} = \frac{1}{2} \int d^3 \mathbf{x} \left[\pi^2 + (\nabla_i v)(\nabla^i v) + \frac{z''}{z} v^2 \right], \quad (6)$$

where the canonical momentum is given by $\pi \equiv \delta S_2/\delta v'$ as usual. In Fourier space, the equations of motion for each of the Mukhanov-Sasaki modes are

$$v_{\mathbf{k}}' = \pi_{\mathbf{k}} \,, \tag{7a}$$

$$\pi_{\mathbf{k}}' = -\left(k^2 - \frac{z''}{z}\right)v_{\mathbf{k}}.\tag{7b}$$

From this equation, it is clear that the dynamics of the background field ϕ has an active role in the evolution of the effective oscillation frequency.

Primordial curvature fluctuations emerge as quantummechanical perturbations of the inflaton field. Therefore, we proceed with the canonical quantization of each Fourier mode, in which the canonical variables are promoted to operators. Thus, the Hamiltonian becomes

$$\hat{H}_{\text{sys}} = \int_{\mathbb{R}^{3+}} d^3 \mathbf{k} \left[\hat{\pi}_{\mathbf{k}} \hat{\pi}_{\mathbf{k}}^{\dagger} + \hat{v}_{\mathbf{k}} \left(k^2 - \frac{z''}{z} \right) \hat{v}_{\mathbf{k}}^{\dagger} \right], \quad (8)$$

where the integration region \mathbb{R}^{3+} represents the upper half of the Fourier sphere. Momentum and field operators obey the canonical commutation relation

$$\left[\hat{v}_{\mathbf{k}}, \hat{\pi}_{\mathbf{k}'}^{\dagger}\right] = i\delta^{(3)}(\mathbf{k} - \mathbf{k}'), \qquad (9)$$

as stated in [21], the main problem with this representation is that operators are not Hermitian. To ensure Hermiticity, it is convenient to build a new set of field operators

$$\hat{v}_{\rm R} \equiv \frac{\hat{v}_{\mathbf{k}} + \hat{v}_{\mathbf{k}}^{\dagger}}{\sqrt{2}} \quad , \quad \hat{v}_{\rm I} \equiv \frac{\hat{v}_{\mathbf{k}} - \hat{v}_{\mathbf{k}}^{\dagger}}{i\sqrt{2}},$$
 (10)

where the labels R and I dub the corresponding real and imaginary parts of the field. These definitions extend naturally to the conjugate momentum. As for the dynamics of the operators \hat{v}_R and \hat{v}_I , their evolution is governed by Eqns. (7a) and (7b), as in the case of the original field operators. The canonical commutation rule in (9) imposes similar relations for the real and imaginary components

$$[\hat{v}_{S}(\mathbf{k}), \hat{\pi}_{S'}(\mathbf{k}')] = i\delta_{SS'}\delta^{(3)}(\mathbf{k} - \mathbf{k}'), \qquad (11)$$

where the indices $S, S' \in \{R, I\}$. Notice that the separation into real and imaginary parts does not introduce any new degrees of freedom in the system. Therefore, we can recast the Hamiltonian operator in terms of the real and imaginary field components as

$$\hat{H}_{\text{sys}} = \frac{1}{2} \sum_{S \in \{R,I\}} \int_{\mathbb{R}^{3+}} d^3 \mathbf{k} \left[\hat{\pi}_S \hat{\pi}_S^{\dagger} + \hat{v}_S \left(k^2 - \frac{z''}{z} \right) \hat{v}_S^{\dagger} \right],$$
(12)

where we omitted the k-dependence to shorten the notation. With respect to these canonical variables, the Hamiltonian – together with the other field operators and their combinations– is Hermitian, which guarantees that its expectation values are real. Furthermore, it is important to consider that Minkowski vacuum minimizes the energy and variance for all values of k, and in consequence, it represents the state of quantum fluctuations at subhorizon scales and defines a well-suited set of initial conditions.

At second order in perturbative expansion the Hamiltonian is quadratic in its canonical coordinates, so all of the information of the system is contained in two-point correlation functions. Consequently, Gaussian states provide a complete description of the state of vacuum fluctuations. Moreover, it is well-known that Gaussian states remain Gaussian under linear evolution, and the deformations of the Wigner ellipse¹ – which encloses all possible configurations of a Gaussian state – are limited to shears,

¹ In the Wigner formalism, this ellipse is defined by the bilinear form in the Gaussian Wigner quasi-probability distribution, and can be trivially extended to an arbitrary number of fields, see [20, 32, 33] for further details.

contractions, expansions and rotations. With this in mind, the information of each mode is contained in the following state vector of operators

$$\hat{\mathbf{R}} = (\hat{v}_{\mathrm{R}}, \hat{\pi}_{\mathrm{R}}, \hat{v}_{\mathrm{I}}, \hat{\pi}_{\mathrm{I}})^{\mathrm{T}} , \qquad (13)$$

and all of the two-point correlation functions are encoded in the following matrix of the Minkowski vacuum expectation values

$$\langle \hat{\mathbf{\Sigma}} \rangle \equiv \left\langle \left\{ \hat{\mathbf{R}}, \hat{\mathbf{R}} \right\} \right\rangle = \left\langle \hat{\mathbf{\Sigma}}^{\mathrm{R}} \right\rangle \oplus \left\langle \hat{\mathbf{\Sigma}}^{\mathrm{I}} \right\rangle,$$
 (14)

where the symbol $\{\cdot,\cdot\}$ denotes the anticommutator acting on each component of the operator's state vector $\hat{\mathbf{R}}$. The direct sum in this last identity indicates that cross-correlations between real and imaginary components cancel, which reduces $\langle \hat{\mathbf{\Sigma}} \rangle$ to a block-diagonal matrix containing two 2×2 submatrices for the real and imaginary parts. The lengths of the semimajor and semiminor axes of the Wigner ellipse are the eigenvalues of the covariance matrix, while the rotation angle is determined by their corresponding eigenvectors. Each of the covariance matrices for the real and imaginary parts, $\langle \hat{\mathbf{\Sigma}}^{\mathrm{S}} \rangle$ for $\mathrm{S} \in \{\mathrm{R},\mathrm{I}\}$, has the following form

$$\langle \hat{\mathbf{\Sigma}}^{S} \rangle = \begin{pmatrix} \langle \hat{\Sigma}_{(vv)}^{S} \rangle & \langle \hat{\Sigma}_{(vp)}^{S} \rangle \\ \langle \hat{\Sigma}_{(vp)}^{S} \rangle & \langle \hat{\Sigma}_{(pp)}^{S} \rangle \end{pmatrix} . \tag{15}$$

Explicitly, each of these matrix elements is computed from the vacuum expectation values of the following operators

$$\hat{\Sigma}_{(vv)}^{S} = \{\hat{v}_{S}(\mathbf{k}'), \hat{v}_{S}(\mathbf{k})\}, \qquad (16a)$$

$$\hat{\Sigma}_{(vp)}^{S} = \{\hat{v}_{S}(\mathbf{k}'), \hat{\pi}_{S}(\mathbf{k})\}, \qquad (16b)$$

$$\hat{\Sigma}_{(pp)}^{S} = \{\hat{\pi}_{S}(\mathbf{k}'), \hat{\pi}_{S}(\mathbf{k})\}, \qquad (16c)$$

where $S \in \{R, I\}$ and $k = |\mathbf{k}|$. Therefore, it is clear that these operators correspond to the block-diagonal pieces of the anticommutator $\{\hat{\mathbf{R}}, \hat{\mathbf{R}}\}$ defined in Eq. (14). Standard commutation rules allow us to assign a covariance matrix for each k-mode, which yields

$$\langle \hat{\Sigma}_{(vv)}^{S} \rangle = 2 \langle \hat{v}_{S}(\mathbf{k}), \hat{v}_{S}(\mathbf{k}) \rangle ,$$
 (17a)

$$\langle \hat{\Sigma}_{(vp)}^{S} \rangle = \langle \hat{v}_{S}(\mathbf{k}), \hat{\pi}_{S}(\mathbf{k}) \rangle + \langle \hat{\pi}_{S}(\mathbf{k}), \hat{v}_{S}(\mathbf{k}) \rangle , \qquad (17b)$$

$$\langle \hat{\Sigma}_{(pp)}^{S} \rangle = 2 \langle \hat{\pi}_{S}(\mathbf{k}), \hat{\pi}_{S}(\mathbf{k}) \rangle ,$$
 (17c)

after excluding overall mode fixing factors of $\delta^{(3)}(\mathbf{k}-\mathbf{k}')$. From now on, the index S can be fixed to only refer to the real or the imaginary part of the solution, without losing any information after this choice. We can derive equations of motion for the expectation values by taking derivatives

$$\frac{\mathrm{d}}{\mathrm{d}\tau} \langle \hat{\Sigma}_{(vv)}^{\mathrm{S}} \rangle = 2 \langle \hat{\Sigma}_{(vp)}^{\mathrm{S}} \rangle , \qquad (18a)$$

$$\frac{\mathrm{d}}{\mathrm{d}\tau} \langle \hat{\Sigma}_{(vp)}^{\mathrm{S}} \rangle = \langle \hat{\Sigma}_{(pp)}^{\mathrm{S}} \rangle - \left(k^2 - \frac{z''}{z} \right) \langle \hat{\Sigma}_{(vv)}^{\mathrm{S}} \rangle, \qquad (18b)$$

$$\frac{\mathrm{d}}{\mathrm{d}\tau} \langle \hat{\Sigma}_{(pp)}^{\mathrm{S}} \rangle = -2 \left(k^2 - \frac{z''}{z} \right) \langle \hat{\Sigma}_{(vp)}^{\mathrm{S}} \rangle, \qquad (18c)$$

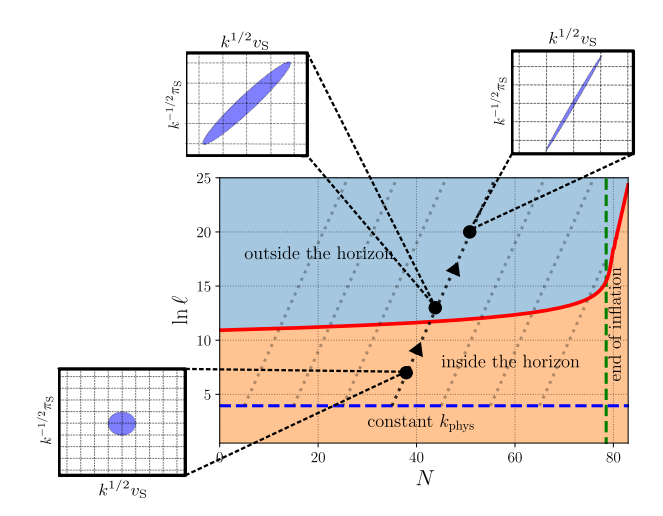


FIG. 2. Evolution scheme for perturbation modes during cosmic inflation. The x-axis shows the number of e-folds, while the y-axis tracks the evolution of physical length scales (ℓ) , including the horizon 1/H (red curve). Approximate timetranslational symmetry permits choosing initial conditions on a surface of large constant physical wavelength $k_{\rm phys}$. Lateral insets illustrate the deformation of the Wigner ellipse at different times, shown in dimensionless units. The evolution reflects the squeezing of the ellipse as modes cross the horizon.

or, equivalently, by replacing the covariance matrix operators (for every fixed $\bf k)$ defined in Eqns. (16a–16c) in the Liouville equation

$$\frac{\mathrm{d}}{\mathrm{d}\tau} \langle \hat{\mathbf{\Sigma}}^{\mathrm{S}} \rangle = i \left\langle \left[\hat{H}_{\mathrm{sys}}, \hat{\mathbf{\Sigma}}^{\mathrm{S}} \right] \right\rangle. \tag{19}$$

Equations (18a–18c) can be combined into a single thirdorder transport equation for the covariance component $\langle \hat{\Sigma}_{(sv)}^{S} \rangle$:

$$\frac{\mathrm{d}^{3}}{\mathrm{d}\tau^{3}}\langle\hat{\Sigma}_{(vv)}^{\mathrm{S}}\rangle + 4\left(k^{2} - \frac{z''}{z}\right)\frac{\mathrm{d}}{\mathrm{d}\tau}\langle\hat{\Sigma}_{(vv)}^{\mathrm{S}}\rangle$$

$$+2\left[\left(k^{2} - \frac{z''}{z}\right)'\langle\hat{\Sigma}_{(vv)}^{\mathrm{S}}\rangle\right] = 0,$$
(20)

which only holds if the real and imaginary modes are solutions to the mode equations in Eqns. (7a) and (7b), and also implies that it can be order-reduced.

The interpretation of the averaged covariance matrix elements is crucial, since the Wigner ellipse is defined by this Hermitian positive-definite matrix. This ellipse encloses the mode configurations accessible for each value of k. Moreover, the determinant of $\langle \hat{\Sigma}^{\hat{S}} \rangle$

$$S \equiv \det\langle \hat{\mathbf{\Sigma}}^{S} \rangle \,, \tag{21}$$

is the area of the Wigner ellipse and, in the case of an isolated system, needs to be conserved throughout the entire mode evolution.

In Figure 2, we present an evolution scheme of modes that takes advantage of the invariance of the vacuum

state on deep subhorizon scales [27, 28]. This approximate symmetry allows us to avoid evolving high-frequency modes over long timescales, during which the state remains effectively unchanged. The relation $k = k_{\rm phys}a$ enables us to initialize modes (plotted in dashed black lines) with different comoving wavevectors after N e-folds of background expansion. The end of mode evolution is denoted in the figure by the dashed green vertical, which denotes when the slow-roll parameter ϵ equals to one. The side insets of the figure illustrate the deformation of the Wigner ellipse for an arbitrarily chosen mode as it crosses the horizon. The ellipse squeezing process is characterized by the exponential growth of the semimajor axis and a corresponding contraction of the semiminor axis. Hence, horizon crossing is an effective way to produce squeezed states without breaking unitary evolution. However, this behavior is a complication for straightforward numerical implementations of Eqns. (18a–18c), which are prone to develop instabilities if the conservation of \mathcal{S} (i.e., the area of the ellipse) is not carefully preserved during the exponential squeezing phase. Such instabilities can be exacerbated by state deformations induced by decoherence, or by increasing the number of degrees of freedom.

With the initial part of the formalism in place, it is possible to compute the power spectrum of primordial curvature fluctuations $\mathcal{P}_{\zeta}(k)$ by returning to the gauge-invariant curvature fluctuation $\hat{\zeta}_{\mathbf{k}}$

$$\mathcal{P}_{\zeta}(k) = \frac{k^3}{4\pi^2} \left(\frac{H^2}{a^2 \dot{\phi}^2} \right) \langle \hat{\Sigma}_{(vv)}^{S} \rangle. \tag{22}$$

While not practical, the corresponding transport equation for the curvature power spectrum can be obtained by replacing this definition in Eq. (20).

B. Two-point correlators of a system coupled to an environment

Thus far, we have reviewed the fundamentals of inflation driven by a single scalar field. In this subsection, we follow the open system formalism developed in [18–22] to

examine the simplest form of coupling between the field fluctuation modes and an environment, and to analyze its impact on the dynamics of inflationary two-point correlators. Thus, to provide a preliminary notion of such an interaction, we write the form of the total Hamiltonian

$$\hat{H}_{\text{tot}} = \hat{H}_{\text{svs}} \otimes \hat{\mathbb{1}}_{\text{env}} + \hat{\mathbb{1}}_{\text{svs}} \otimes \hat{H}_{\text{env}} + g\hat{H}_{\text{int}}, \qquad (23)$$

where $\hat{H}_{\rm sys}$ is the system Hamiltonian introduced in Eq. (12), g is the coupling constant and $\hat{H}_{\rm int}$ encodes the interaction between the system and the environment. We assume that the interaction term is separable (as the rest of the Hamiltonian). Hence, it can be cast in the form

$$\hat{H}_{\rm int}(\tau) = \int_{\mathbb{R}^{3+}} d^3 \mathbf{k} \ \hat{I}_{\mathbf{k}}(\tau) \otimes \hat{E}_{-\mathbf{k}}(\tau) , \qquad (24)$$

where $\hat{I}_{\mathbf{k}}$ is an operator acting on the system states, while $\hat{E}_{-\mathbf{k}}$ acts on the environment states. The effects of such interactions are confined to specific bands of length scales, and their spatial realizations are consistent with either fine- or coarse-graining. The interaction operators can also be decomposed into their real and imaginary parts in the same way as the field and momentum operators.

As stated in the previous subsection, the complete characterization of a Gaussian state is given by the expectation values of the covariance matrix operators. Obtaining these requires tracing over the environmental degrees of freedom to construct the reduced density operator

$$\hat{\rho}_{\text{sys}} = \text{Tr}_{\text{env}} \left[\hat{\rho}_{\text{tot}} \right] \,, \tag{25}$$

which serves as a starting point for evaluating the expectation values of the operators defined in Eqns. (16a-16c)

$$\langle \hat{\mathbf{\Sigma}}^{\mathrm{S}} \rangle = \mathrm{Tr} \left[\hat{\rho}_{\mathrm{sys}} \hat{\mathbf{\Sigma}}^{\mathrm{S}} \right] ,$$
 (26)

thereby yielding the quantities that fully specify the Gaussian state.

Under the assumption of a nearly stationary environment, we consider that the evolution of covariance matrix is governed by the Lindblad equation in Fourier domain (see [34] for a complete derivation)

$$\frac{\mathrm{d}}{\mathrm{d}\tau} \langle \hat{\mathbf{\Sigma}}^{\mathrm{S}} \rangle = -i \left\langle \left[\hat{\mathbf{\Sigma}}^{\mathrm{S}}, \hat{H}_{\mathrm{sys}} \right] \right\rangle - (2\pi^{3})^{1/2} \Gamma \int_{\mathbb{R}^{3+}} d^{3}\mathbf{k} \ \tilde{C}_{E}(\mathbf{k}, \tau) \left\langle \left[\left[\hat{\mathbf{\Sigma}}^{\mathrm{S}}, \hat{I}_{\mathbf{k}}^{\mathrm{S}} \right], \hat{I}_{\mathbf{k}}^{\mathrm{S}} \right] \right\rangle , \tag{27}$$

where $\Gamma \equiv 2g^2\tau_{\rm c}$ is the decay rate considering the autocorrelation time $\tau_{\rm c}$ to be small compared to the characteristic timescales of the environment. The quantity $\tilde{C}_E(\tau,k)$ denotes the power spectrum of the environmental interaction operator \hat{E} , i.e., $\langle |\hat{E}_{\bf k}(\tau)|^2 \rangle$, assumed to be statistically homogeneous. This term results from tracing over the eigenstates of $\hat{E}_{-\bf k}$, and acts dissipatively due

to the hermiticity of all the operators involved. A preliminary physical interpretation is that the environment's power spectrum effectively acts as a source term for the system's power spectrum. Obtaining solutions for the general form of the interaction operators is a challenging task. However, in the regime where the Wigner function is expected to remain Gaussian throughout the evolution, the interaction operator reduces to a linear combination of the field and its conjugate momentum

$$\hat{I}_{\mathbf{k}}^{S} = \alpha(\tau)\hat{v}_{\mathbf{k}}^{S} + \beta(\tau)\hat{\pi}_{\mathbf{k}}^{S}, \qquad (28)$$

which greatly simplifies the derivation of transport equations for the covariance matrix. In this case, it suffices to solve the particular case $\alpha(\tau)=1$ and $\beta(\tau)=0$ to obtain the transport equations for a general linear combination. Fixing $\hat{I}_{\bf k}^{\rm S}=\hat{v}_{\bf k}^{\rm S}$, and substituting the operator definitions from Eqns. (16a–16c) yields

$$\frac{\mathrm{d}}{\mathrm{d}\tau} \langle \hat{\Sigma}_{(vv)}^{\mathrm{S}} \rangle = 2 \langle \hat{\Sigma}_{(vp)}^{\mathrm{S}} \rangle, \qquad (29a)$$

$$\frac{\mathrm{d}}{\mathrm{d}\tau} \langle \hat{\Sigma}_{(vp)}^{\mathrm{S}} \rangle = \langle \hat{\Sigma}_{(pp)}^{\mathrm{S}} \rangle - \left(k^2 - \frac{z''}{z} \right) \langle \hat{\Sigma}_{(vv)}^{\mathrm{S}} \rangle, \qquad (29b)$$

$$\frac{\mathrm{d}}{\mathrm{d}\tau} \langle \hat{\Sigma}_{(pp)}^{\mathrm{S}} \rangle = -2 \left(k^2 - \frac{z''}{z} \right) \langle \hat{\Sigma}_{(vp)}^{\mathrm{S}} \rangle + 2\mathcal{F}(k,\tau) , \quad (29c)$$

where $\mathcal{F}(k,\tau) \equiv (2\pi)^{3/2} \Gamma \tilde{C}_E(k,\tau)$. After assigning a wavevector \mathbf{k} , it is safe to omit writing $\delta^{(3)}(\mathbf{k}-\mathbf{k}')$ in the last term at the right hand side of (29c). The case of a general linear combination given by Eq. (28) provides a useful framework for exploring momentum-dependent couplings to an environment. Such couplings are particularly relevant when constructing effective inflationary models with kinetic deformations [17]. In these and other scenarios, one finds that the corresponding transport equations retain the same form as in Eqns. (29a–29c) provided that the following variable redefinitions are applied

$$\langle \hat{\Sigma}_{(vv)}^{S} \rangle \to \overline{\langle \hat{\Sigma}_{(vv)}^{S} \rangle} = \langle \hat{\Sigma}_{(vv)}^{S} \rangle,$$
 (30a)

$$\langle \hat{\Sigma}_{(vp)}^{S} \rangle \to \overline{\langle \hat{\Sigma}_{(vp)}^{S} \rangle} = \langle \hat{\Sigma}_{(vp)}^{S} \rangle + \beta^{2}(\tau) \mathcal{F}(k, \tau) ,$$
 (30b)

$$\langle \hat{\Sigma}_{(pp)}^{S} \rangle \to \overline{\langle \hat{\Sigma}_{(pp)}^{S} \rangle} = \langle \hat{\Sigma}_{(pp)}^{S} \rangle - 2\alpha(\tau)\beta(\tau)\mathcal{F}(k,\tau) + \frac{\mathrm{d}}{\mathrm{d}\tau} \left[\beta^{2}(\tau)\mathcal{F}(k,\tau) \right] , \tag{30c}$$

$$\mathcal{F} \to \overline{\mathcal{F}}(k,\tau) = \left[\alpha^2(\tau) + \beta^2(\tau) \left(k^2 - \frac{z''}{z}\right)\right] \mathcal{F}(k,\tau) - \frac{\mathrm{d}}{\mathrm{d}\tau} \left[\alpha(\tau)\beta(\tau)\mathcal{F}(k,\tau)\right] + \frac{1}{2} \frac{\mathrm{d}^2}{\mathrm{d}\tau^2} \left[\beta^2(\tau)\mathcal{F}(k,\tau)\right] . \tag{30d}$$

Therefore, it is possible to consider the same transport equation and perform an additional change of variables to study other forms of coupling. As in the case of isolated systems (e.g., Eq. (20)), it is possible to condense the transport equations with respect to the redefined variables into a single third-order differential equation for the field correlator

$$\left\{ \frac{\mathrm{d}^3}{\mathrm{d}\tau^3} + 4\left(k^2 - \frac{z''}{z}\right) \frac{\mathrm{d}}{\mathrm{d}\tau} + 2\left(k^2 - \frac{z''}{z}\right)' \right\} \langle \hat{\Sigma}_{(vv)}^{\mathrm{S}} \rangle = 4\mathcal{F}(k,\tau), \tag{31}$$

where we omitted the bars for conciseness in the notation. This expression is consistent with the notion of the environment's power spectrum acting as a source term for the power spectrum of the system. Furthermore, if we compute the time derivative of the covariance matrix using the transport equation, we can gain a deeper understanding into the role of this source term

$$\frac{\mathrm{d}}{\mathrm{d}\tau} \mathcal{S} = 2\langle \hat{\Sigma}_{(vv)}^{\mathrm{S}} \rangle \mathcal{F}(k,\tau) , \qquad (32)$$

which implies that $\mathcal{F}(k,\tau)$ controls the size of the Wigner ellipse. Similarly, the results in [21] show that the source term affects the evolution of all squeezing parameters, albeit in distinct ways. Among these deformations, the dominant effect is the variation in the enclosed area, which offers the most direct signature of information exchange

with the environment.².

So far, previous studies have proposed different forms of the source term $\mathcal{F}(k,\tau)$ following diverse physical motivations. A conservative choice is to restrict its action to the ultraviolet regime [34], thereby avoiding low-frequency observational signatures. In the extreme ultraviolet limit, this choice can also serve as a tool to explore implications of the Trans-Planckian Censorship Conjecture (TCC) [35, 36]. Extensions that incorporate infrared effects – by considering a window function instead of a smoothened step – have also been used to study CMB constraints on real-space entanglement [20]. In contrast, our objective is to generate a flexible framework for generating

² From a thermodynamic standpoint, such variations modify the number of accessible states and, consequently, the production of entropy for the system.

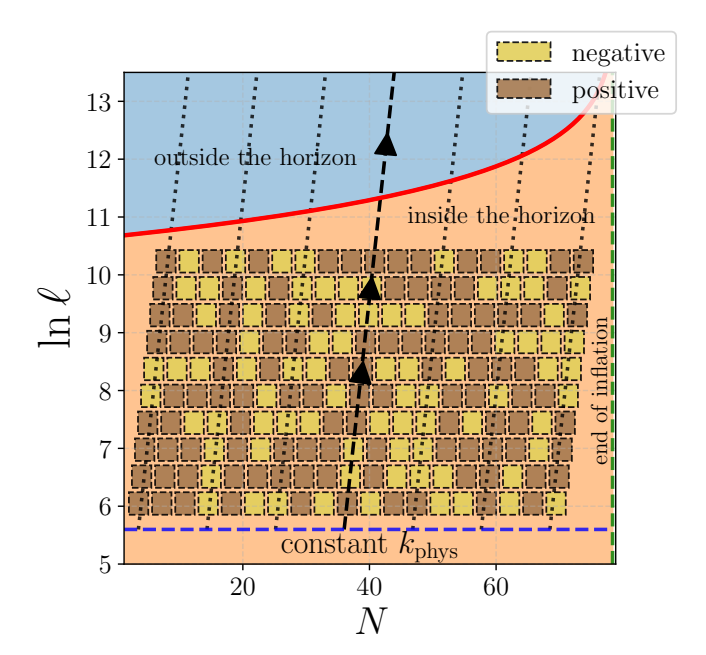


FIG. 3. Example of an arbitrary configuration of decoherence events ("accidents") in a portion of the $(N, \ln \ell)$ plane. These accidents are arranged as "tiles" within a region bounded above by the horizon and below by a surface of constant $k_{\rm phys}$. The source term can either increase or reduce the determinant of the covariance matrix. This setup enables the evaluation of an arbitrary time-dependent power spectrum of the environment.

events in a broad range of frequencies and durations. As a preliminary step, we recall that each physical wavelength ℓ observed after N e-folds of inflation corresponds to a comoving wavenumber $k=e^N/\ell$. Similarly, for subhorizon evolution, the conformal time is given by $\tau=\int H^{-1}e^{-N}dN$ as a function of N. This allows us to recast the source term $\mathcal{F}(k,\tau)$ with respect to $\ln \ell$ and N, which naturally captures physical scales and their evolution during inflation. We then propose the following functional form

$$\mathcal{F}(k,\tau) = \tag{33}$$

$$\sum_{i=1}^{n_{\ell}} \sum_{i=1}^{n_{N}} A(\ln \ell_{j}, N_{i}) \ T\left(\frac{N - N_{i}}{\Delta N_{ij}}\right) \kappa\left(\frac{\ln \ell - \ln \ell_{j}}{\Delta \ell_{ij}}\right),$$

which partitions the region between the horizon and constant physical wavelength into an array of $n_\ell \times n_N = n_{\rm tiles}$ events distributed like "tiles" in that region of the $(N, \ln \ell)$ plane. The amplitude of each tile, $A(\ln \ell_j, N_i)$, is given by

$$A(\ln \ell_j, N_i) = \frac{\exp[(p-1)N_i]}{(2\pi^3)^{1/2}\ell_i^2} \alpha_{\Gamma}(\ln \ell_j, N_i), \qquad (34)$$

where $\alpha_{\Gamma}(\ln \ell_j, N_i)$ is a dimensionless function specifying the strength of the environmental effect for the tile (i, j). This expression is obtained from the amplitude

prescription for a single accident given, for example, in [34], after transforming to the $(N, \ln \ell)$ variables. Here, $\ln \ell_i$ denotes the logarithm of the physical length scale at which the accident is most effective, N_i is the number of e-folds where the tile is located, and p controls the steepness of the event. A key feature of our approach is that $\alpha_{\Gamma}(\ln \ell_i, N_i)$ may take positive and negative values, representing, respectively an increase or a decrease in the number of available states encoded in each Wigner ellipse. For the evolution of Gaussian states described in Eqns. (29a-29c), negative values α_{Γ} do not violate the positivity of the Wigner function, except when the covariance matrix becomes singular. The functions T(N) and $\kappa(\ln \ell)$ behave as window functions centered at N_i and $\ln \ell_i$, respectively, with the widths of the corresponding length and time bands for the tile (i, j), given by ΔN_{ij}

Using the same mode injection scheme depicted in Figure 2, in Figure 3 we illustrate an example configuration of decoherence accidents consistent with our proposal for the source term $\mathcal{F}(k,\tau)$ in Eq. (33). Such a setup offers several possibilities of interest, for example: (1) it reformulates the mode-evolution problem as an analogue of a scattering process, in which each mode may undergo multiple accidents throughout its evolution, with the primary interest placed on the characteristics of the resulting output state; (2) it enables the preparation of arbitrary initial Gaussian states to investigate the emergence of features in the primordial power spectrum of curvature fluctuations across different frequencies; (3) and it accommodates more general configurations that capture the effects of an evolving environment across different scales. With these possibilities in mind, we must design optimized numerical routines that guarantee stable solutions to the transport equations without compromising computational efficiency. The implementation and validation of our approach are detailed in the following subsection.

Figure 3 reveals that, in principle, it is possible to configure decoherence sequences containing accidents in which α_{Γ} becomes negative. This regime admits several interpretations, ranging from apparent violations of the uncertainty principle to effective theories defined on specific projections of the Wigner ellipse rather than in the complete phase-space volume. These and other scenarios may also be incorporated with the purpose of controlling initial state deformations in a more precise way.

C. Implementation of fast and slow component separation for single field models

Until now, we summarized the main steps required to derive the transport equations in (29a-29c), which independently evolve each Fourier mode of the two-point correlators in the presence of decoherence events. These equations can be recast in terms of the original correlators

$$\frac{\mathrm{d}}{\mathrm{d}\tau} \langle \hat{v}_{\mathrm{S}}, \hat{v}_{\mathrm{S}} \rangle = \langle \hat{v}_{\mathrm{S}}, \hat{\pi}_{\mathrm{S}} \rangle + \langle \hat{\pi}_{\mathrm{S}}, \hat{v}_{\mathrm{S}} \rangle, \tag{35a}$$

$$\frac{\mathrm{d}}{\mathrm{d}\tau} \left[\langle \hat{v}_{\mathrm{S}}, \hat{\pi}_{\mathrm{S}} \rangle + \langle \hat{\pi}_{\mathrm{S}}, \hat{v}_{\mathrm{S}} \rangle \right] = 2 \left[\langle \hat{\pi}_{\mathrm{S}}, \hat{\pi}_{\mathrm{S}} \rangle - \left(k^2 - \frac{z''}{z} \right) \langle \hat{v}_{\mathrm{S}}, \hat{v}_{\mathrm{S}} \rangle \right], \tag{35b}$$

$$\frac{\mathrm{d}}{\mathrm{d}\tau} \langle \hat{\pi}_{\mathrm{S}}, \hat{\pi}_{\mathrm{S}} \rangle = -\left(k^2 - \frac{z''}{z}\right) \left[\langle \hat{v}_{\mathrm{S}}, \hat{\pi}_{\mathrm{S}} \rangle + \langle \hat{\pi}_{\mathrm{S}}, \hat{v}_{\mathrm{S}} \rangle\right] + \mathcal{F}(k, \tau). \tag{35c}$$

A crucial aspect in our analysis is that all the operators are Hermitian, and their corresponding expectation values are real. This allows substituting the quantum field operators by rescaled Gaussian random variables spanning the spectrum of real field values. In the case of $\hat{v}_{\rm S}$, this substitution yields

$$\hat{v}_{\rm S} \to L_k \tilde{\chi}_{\rm S} \,, \tag{36}$$

where the quantity $\tilde{\chi}$ is a unit Gaussian random variable, and in the isolated case, each possible expectation value is a solution to the mode equations in (7a-7b).³ By direct substitution in the Lindblad equation, it is straightforward to check that this equations also govern the dynamics of one-point functions. L_k is a real rescaling factor, which is consistent with the field amplitude. In the same way, we compute the corresponding form of the momentum operator

$$\hat{\pi}_{\rm S} \to L_k' \tilde{\chi}_{\rm S} + L_k \tilde{\chi}_{\rm S}',$$
 (37)

where, in contrast with previous work - e.g., [37] -, we consider dynamical random variables. Normalization of random variables introduces a gauge condition

$$\langle \tilde{\chi}_{\rm S}, \tilde{\chi}_{\rm S} \rangle = 1,$$
 (38)

which, when replaced in Eq. (35a) together with the field ansatz in (36) and (37), yields the following consistency relation

$$\frac{\mathrm{d}}{\mathrm{d}\tau} \langle \tilde{\chi}_{\mathrm{S}}, \tilde{\chi}_{\mathrm{S}} \rangle = \langle \tilde{\chi}'_{\mathrm{S}}, \tilde{\chi}_{\mathrm{S}} \rangle + \langle \tilde{\chi}_{\mathrm{S}}, \tilde{\chi}'_{\mathrm{S}} \rangle = 0, \qquad (39)$$

which imposes the gauge condition at all times. This normalization condition ensures that the field correlator $\langle \hat{v}_{\rm S}, \hat{v}_{\rm S} \rangle$ remains equal to L_k^2 at all times. In a way reminiscent of mode evolution for isolated systems, the evolution of L alone is sufficient to determine this correlator. At the same time, as noted in the previous subsection, numerically evolving the field correlators via Eqns. (35a–35c) can develop instabilities. A natural next step is therefore to reformulate the transport equations in terms of L_k and

other derivatives of the random-variable correlators. To proceed with this step, we substitute into Eq. (35b) the field redefinitions, the gauge condition in (38), and its consistency relation in (39), obtaining

$$\left[\frac{\mathrm{d}^2}{\mathrm{d}\tau^2} + \left(k^2 - \frac{z''}{z}\right) - \langle \tilde{\chi}_{\mathrm{S}}', \tilde{\chi}_{\mathrm{S}}' \rangle\right] L_k = 0.$$
 (40)

To close the system, we need to find the equation of motion for the correlator $\langle \tilde{\chi}'_{\rm S}, \tilde{\chi}'_{\rm S} \rangle$. This follows from substituting the above relations, together with Eq. (40), into Eq. (35c):

$$\frac{\mathrm{d}}{\mathrm{d}\tau}\langle \tilde{\chi}'_{\mathrm{S}}, \tilde{\chi}'_{\mathrm{S}} \rangle = -\frac{4L'_{k}}{L_{k}}\langle \tilde{\chi}'_{\mathrm{S}}, \tilde{\chi}'_{\mathrm{S}} \rangle + \frac{1}{L_{k}^{2}} \mathcal{F}(k, \tau). \tag{41}$$

We thus arrive at a second-order system of ordinary differential equations – rather than the third-order equation in Eq. (31) – representing a minor modification to the Ermakov-Pinney nonlinear equation used in [28] to evolve correlators, and is analog to a mode decomposition in polar coordinates. Notably, although real Gaussian random variables commute, this property is not required for deriving Eqns. (40) and (41).

A complete description of the dynamical system requires initial conditions, set at the surface of constant physical wavelength

$$L_k|_{\tau=\tau_0} = \left[4\left(k^2 - \frac{z''}{z}\right)\right]_{\tau=\tau_0}^{-1/4},$$
 (42a)

$$L'_{k}|_{\tau=\tau_{0}}=0,$$
 (42b)

$$\langle \hat{\chi}'_{\mathrm{S}}, \hat{\chi}'_{\mathrm{S}} \rangle |_{\tau = \tau_0} = k^2 - \frac{z''}{z} \Big|_{\tau = \tau_0},$$
 (42c)

which are built to match standard Minkowski vacuum deep inside the horizon. By construction, the choice for the "velocity" correlators $\langle \tilde{\chi}'_{\rm S}, \tilde{\chi}'_{\rm S} \rangle$ makes the oscillation frequency in Eq. (40) vanish exactly at $\tau=\tau_0$. Moreover, these correlators evolve according to first-order differential equations, making them computationally inexpensive to solve. This combination – the suppression of the net oscillation frequency and the reduced cost of computing random-variable velocity correlator dynamics – damps oscillations in the evolution of L_k , and permits larger time steps when resolving field correlators on deep subhorizon scales. With these initial conditions, we obtain

³ Note that these substitutions concern only the real expectation values inside the Wigner ellipse, not the usual complex mode expansion of quantum field theory.

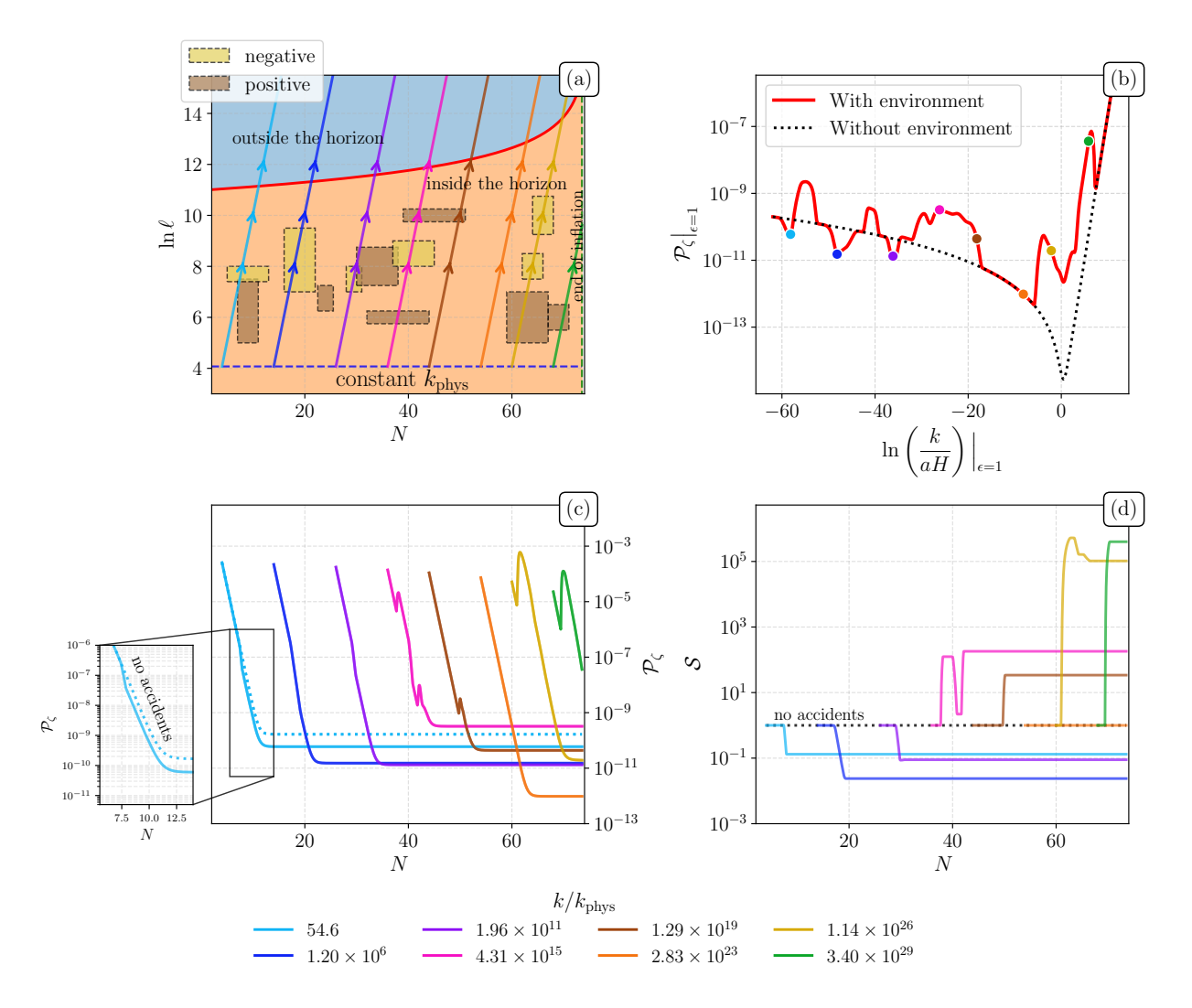


FIG. 4. Implementation of a random distribution of accidents spanning different wavenumber ranges and durations. We use the same color convention as in Figure 3 to denote accidents with positive α_{Γ} in different tones of brown, and yellow in the cases with $\alpha_{\Gamma} < 0$. Panel (a): Distribution of accidents together with the mode injection scheme. Several modes are selected to evaluate their evolution, their contribution to the power spectrum, and the resulting gain or loss in state availability. Panel (b): Power spectrum of primordial curvature fluctuations. The red curve corresponds to the spectrum in the presence of accidents, while the black dotted curve shows the spectrum free of decoherence events. Panel (c): Evolution of the curvature spectrum at fixed wavenumber. Dotted lines depict the evolution with no accidents highlighting how accidents alter the mode dynamics. The inset on the left depicts the reduction of amplitude caused by negative changes in the determinant. Panel (d): Changes in the area of the Wigner ellipse for several modes. The label "no accidents" refers to the conservation of the determinant in the accident-free scenarios. In contrast, decoherence events with finite duration modify the determinant during their action but leave it unchanged once they switch off.

the evolution of the velocity correlators

$$\frac{\langle \tilde{\chi}'_{\rm S}, \tilde{\chi}'_{\rm S} \rangle}{\langle \tilde{\chi}'_{\rm S}, \tilde{\chi}'_{\rm S} \rangle|_{\tau_0}} = \frac{L_k|_{\tau_0}}{L_k^4} \left[1 + \Delta_p(k, \tau) \right] , \qquad (43)$$

$$\Delta_p(k, \tau) = \int_{\tau_0}^{\tau} d\tau' \frac{L_k^2 \mathcal{F}(k, \tau')}{L_k^4|_{\tau_0} \langle \tilde{\chi}'_{\rm S}, \tilde{\chi}'_{\rm S} \rangle|_{\tau_0}} ,$$

where $\Delta_p(k,\tau)$ captures the contribution from the particular solution of Eq. (41), that the source term generates. From this result, we derive the equation of motion for the

correlation factors L_k :

$$\left[\frac{\mathrm{d}^2}{\mathrm{d}\tau^2} + \left(k^2 - \frac{z''}{z}\right) - \frac{L_k|_{\tau_0}}{L_k^4} \langle \tilde{\chi}_{\mathrm{S}}', \tilde{\chi}_{\mathrm{S}}' \rangle|_{\tau_0} - \frac{L_k|_{\tau_0}}{L_k^4} \langle \tilde{\chi}_{\mathrm{S}}', \tilde{\chi}_{\mathrm{S}}' \rangle|_{\tau_0} \Delta_p(k, \tau)\right] L_k = 0.$$
(44)

The first line reproduces the usual operator form of the Ermakov-Pinney equation in the case of isolated systems. The extra term proportional to Δ_p actively modifies the dynamics of L_k : it may not only reproduce effects usually attributed to interactions with external fields, but

it can also mimic changes in the background geometry, such as those arising from the expansion history, via a wavenumber-dependent redefinition of z''/z

$$\left[\frac{\mathrm{d}^2}{\mathrm{d}\tau^2} + \left(k^2 - \frac{z_{\text{eff}}''}{z_{\text{eff}}}\right) - \frac{L_k|_{\tau_0}}{L_k^4} \langle \tilde{\chi}_{\mathrm{S}}', \tilde{\chi}_{\mathrm{S}}' \rangle|_{\tau_0}\right] L_k = 0,$$

$$\frac{z_{\text{eff}}''}{z_{\text{eff}}} \equiv \frac{z''}{z} + \frac{L_k|_{\tau_0}}{L_k^4} \langle \tilde{\chi}_{\mathrm{S}}', \tilde{\chi}_{\mathrm{S}}' \rangle|_{\tau_0} \Delta_p(k, \tau).$$
(45)

In this way, the open-systems framework provides a versatile tool to build effective descriptions of inflationary dynamics [38]. The dependence of the last expression on L_k suggests that the description is scale-dependent and may also be potentially affected by backreaction effects.

Based on the description of the system's dynamical variables, we recast the form of the covariance matrix $\langle \Sigma^{\rm S} \rangle$ – as defined in Eq. (15) – in terms of the correlation amplitude L_k and the velocity correlators for an arbitrary k

$$\langle \hat{\Sigma}^{S} \rangle = \begin{bmatrix} \langle \hat{\Sigma}_{(vv)}^{S} \rangle & \langle \hat{\Sigma}_{(vp)}^{S} \rangle \\ \langle \hat{\Sigma}_{(vp)}^{S} \rangle & \langle \hat{\Sigma}_{(pp)}^{S} \rangle \end{bmatrix},$$

$$= 2 \begin{bmatrix} L_{k}^{2} & L_{k}L_{k}' \\ L_{k}L_{k}' & (L_{k}')^{2} + L_{k}^{2}\langle \tilde{\chi}_{S}', \tilde{\chi}_{S}' \rangle \end{bmatrix},$$

$$(46)$$

and find its determinant

$$S = 4L_k^4 \langle \tilde{\chi}_S', \tilde{\chi}_S' \rangle, \tag{47}$$

which, in the absence of decoherence events, needs to be conserved through the entire evolution. The derivative of the determinant in Eq. (32) naturally motivates the interpretation of the source term $\mathcal{F}(k,\tau)$ as an analogue of a torque in classical mechanics, responsible for inducing a sudden change in the angular momentum. In the present context, the counterpart of the angular momentum (squared) is given by the determinant of the covariance matrix.

After setting up the equations of motion, initial conditions and the array of decoherence events represented as "tiles", the results in Figure 4 present the mode evolution scheme for an arbitrary array of decoherence and recoherence events (panel (a)). The effects of this configuration are further represented in panel (b), in the form of features in the power spectrum of primordial fluctuations, where it is compared with the accident-free case. After selecting a few representative modes from the injection scheme in panel (a), panel (c) displays modifications in the mode evolution at fixed values of k, which arise directly from the introduction of accidents at subhorizon scales. To check if mode evolution is stable, panel (d) illustrates the evolution of the Wigner ellipse area – i.e., S – for each Fourier mode, which also makes evident the gain or loss of area as the modes traverse the tiles.

As indicated in Eq. (34), the magnitude of the accident represented by each tile of panel (a) is governed by both the parameter α_{Γ} and the dependence of $A(\ln \ell_j, N_i)$ on the scale factor via p. In this specific case, we considered

 $\alpha_{\Gamma} \in [-0.37; 0.29]$ in the low-k regime, and values up to $\alpha_{\Gamma} = 3.3$ in the high-k tail, close to the end of inflation. Negative values of α_{Γ} are of particular interest, as they can be interpreted as modeling entropy outflows from the system to the environment. However, these scenarios require careful treatment, since such values – or the superposition of negative-valued tiles active at different times – may also drive the determinant towards cancellation, thereby rendering it ill-defined.

To specify the functional forms of T and κ in Eq. (33), we employed cosine tampered window functions. Nonetheless, the implementation is sufficiently general to allow alternative shapes, enabling us to model smooth or sharp accidents across the $(N, \ln \ell)$ plane. Regarding the values of p, we found $p \sim 3$ adequate to control the relevant accident magnitudes, and thus adopted $p \in [2.8; 3.1]$. In contrast with the schematic tiling approach suggested in Figure 3, we assigned different positions, widths and heights for each tile in order to demonstrate that the approach is flexible enough to accommodate a variety of possible distributions of decoherence events.

Figure 4, panel (b) illustrates how different arrays of tiles can be used to generate distinct features in the power spectrum across various ranges of k. Such features can be exploited in phenomenological or statistical studies. For comparison, the dotted black line corresponds to the accident-free case, obtained from the nonlinear potential $V(\phi) = \lambda \phi^4/4$ with $\lambda = 2 \times 10^{-14}$ and initial conditions chosen to produce 73 e-folds of inflation (approx.). Relative to this reference, the presence of accidents can either enhance or suppress the power in specific wavenumber bands (expressed in units of $k_{\rm phys} = 10^3 H_0$, with H_0 fixed as an initial condition). Colored dots, following the color code in the legend, indicate the contribution of individual modes to the final power spectrum. The numerical implementation permits any other single-field inflationary setup to produce features displayed in more intricate models of inflation.

Modifications in the subhorizon evolution of modes for various wavenumbers k are presented in Figure 4, panel (c). Decoherence effects displace the modes from their unperturbed trajectories, leading to either an amplification or suppression of power by several orders of magnitude. For single-field inflation, no transfer of power occurs after horizon crossing, and hence no further deviations arise. As we will explicitly show by the end of this section, the open-system formalism can be used to reproduce specific features in the primordial power spectrum, which are commonly attributed to multifield models. An additional application of this framework is the controlled generation of deformed states, where short evolution timescales combined with ad-hoc sequences of decoherence events are sufficient to deform the Wigner ellipse as required. Furthermore, the results of this panel provide indirect evidence that introducing multiple decoherence events does not necessarily lead to pathological behavior in their subsequent mode evolution. This can be understood from the definition of P_{ζ} , which is proportional to L_k^2 (from

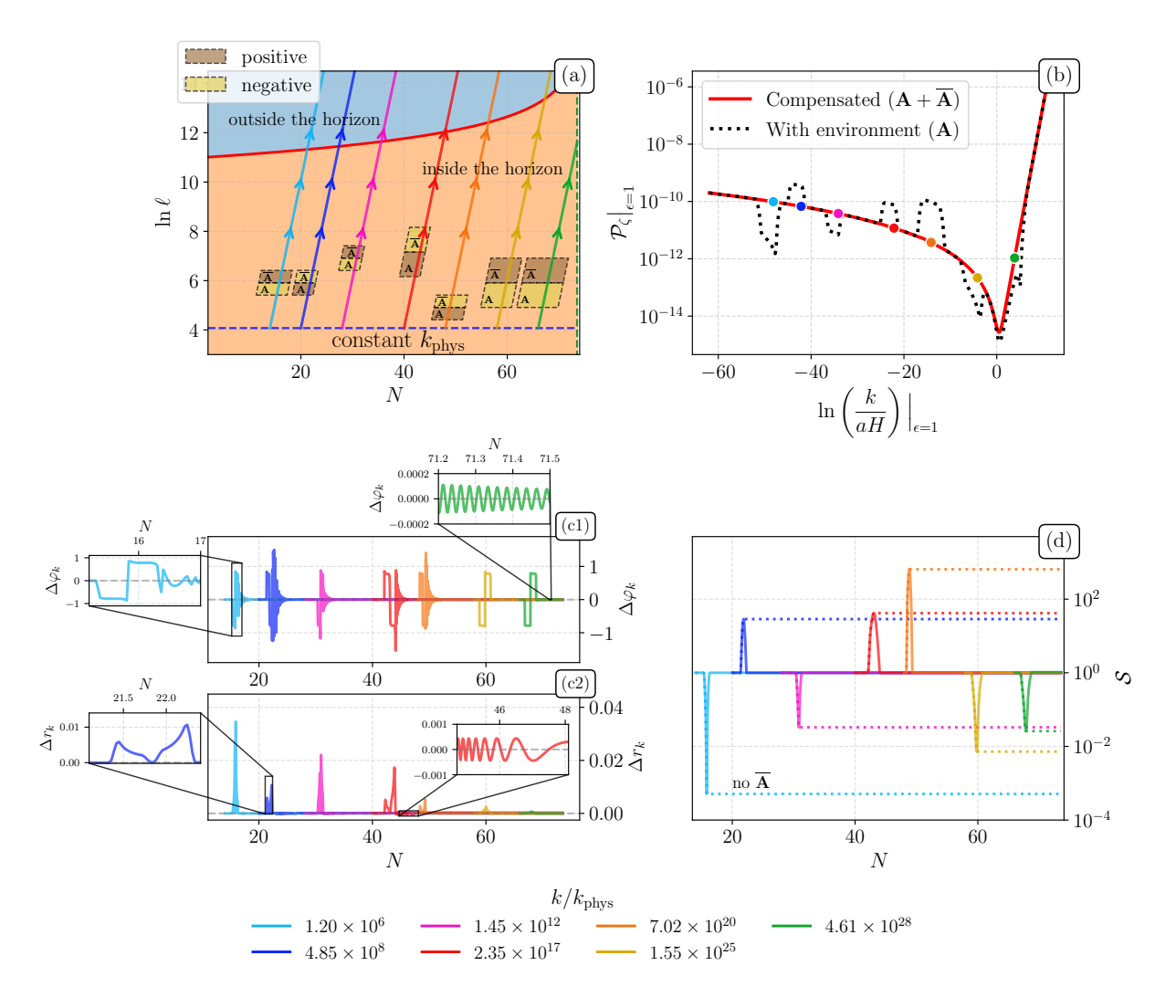


FIG. 5. Implementation of a distribution of decoherence events that leave the primordial power spectrum unaltered. The same color convention as in Figures 3 and 4 is adopted: accidents with positive α_{Γ} are shown in different tones of brown, while those with $\alpha_{\Gamma} < 0$ are shown in yellow. Panel (a): Mode injection scheme and distribution of accidents (A), together with their corresponding anti-accidents (\bar{A}) that cancel effects in mode evolution. We use the source term parameterization proposed in Eq. (48) to confine the effects to specific bands of wavelengths. Panel (b): Power spectrum of primordial curvature fluctuations in the presence of accidents (black dotted line) and after including accident/anti-accident pairs. The compensation mechanism restores the spectrum, leaving it unchanged. Panels (c1) and (c2): Evolution of the deformations in the squeezing parameters $\Delta r_k \equiv r_k - r_k^{(0)}$ and $\Delta \varphi_k \equiv \varphi_k - \varphi_k^{(0)}$, measured relative to the accident-free scenario. The insets show that the final state is represented by a Wigner ellipse with unit area (approx.) and almost negligible eccentricity, which rotates until crossing the horizon. Panel (d): Evolution of the Wigner ellipse area for several modes. After passing through an accident/anti-accident pair, the area relaxes back to unity. The label "no (\bar{A})" indicates cases without anti-accidents, where the enlarged (or reduced) area persists without reversal.

Eqns. (22) and (46)). Since no complex conjugation is involved, the smooth behavior observed in panel (c) directly reflects the dynamics of L_k within the fast-slow separation scheme. In contrast to the standard mode function approach, where the same smoothness arises only from algebraic phase cancellation between complex-conjugate contributions, here the suppression of fast oscillations in the spectrum evolution is a dynamical effect.

The evolution of the Wigner ellipse area is plotted in Figure 4, panel (d) for the same k-modes selected in the

mode injection scheme. The reference mode at $\mathcal{S}=1$ (labeled as "no accidents") confirms the conservation of the determinant in the absence of accidents. Among the other modes, some exhibit growth while others show a reduction in the determinant, yet none display signs of numerical instabilities through their evolution. As noted earlier, cases with negative α_{Γ} (and their superpositions) require careful consideration to account for possible cancellations of the velocity correlator $\langle \hat{\chi}_{\rm S}', \hat{\chi}_{\rm S}' \rangle$ in the determinant, since the numerical evolution breaks as soon as $\mathcal S$ vanishes.

Intermittent decoherence events may also occur without leaving observable traces in the final power spectrum. Nevertheless, they can produce transient modifications of the field variance and thereby lead to nonlinear effects during inflation, including a possible enhancement of non-Gaussianities in models with more complex potentials. To remain compatible with the lack of spectral imprints, their influence on mode evolution must be reversible, which is now possible since we consider accidents with positive or negative values of α_{Γ} . To configure this type of accidents, it is convenient to reparametrize the source term $\mathcal{F}(k,\tau)$ so as to control the specific modes in which the accidents are effective,

$$\mathcal{F}(k,\tau) = \tag{48}$$

$$\sum_{i=1}^{n_{\ell}} \sum_{i=1}^{n_{N}} A(\ln \ell_{j}, N_{i}) T\left(\frac{k - k_{i}}{\Delta k_{ij}}\right) \kappa\left(\frac{\ln \ell - \ln \ell_{j}}{\Delta \ell_{ij}}\right),$$

where Δk_{ij} is the width of the wavenumber band for the tile (i,j). This reparameterization has the effect of transforming the square tiles in Figure 3 into parallelograms by changing the argument of the window function T, and is only a minimal modification of the original prescription in Eq. (33) due to the definition of comoving wavenumbers $k_i = k_{\rm phys} e^{N_i}$. As a next step, we construct an array of decoherence and recoherence events with varying durations, each spanning distinct wavelength bands. To render the overall transformation reversible, each accident needs to be paired with an anti-accident, in which α_{Γ} takes the opposite sign, so that the determinant is reset to its initial value. In Figure 5, we illustrate a concrete implementation of this idea through an arbitrary configuration of reversible decoherence events, where the accidents (A) and anti-accidents (A) are distributed across the mode injection scheme. Panel (a) shows the distribution of accident/anti-accident pairs and the k-modes that traverse them. Panel (b) depicts how the original configuration of accidents deforms the curvature power spectrum, and how this distortion is suppressed by the anti-accidents, restoring the spectrum to its original form. Panels (c1) and (c2) show the evolution of the squeezing parameter variations Δr_k and $\Delta \varphi_k$, defined with respect to their corresponding accident-free values $r_k^{(0)}$ and $\varphi_k^{(0)}$, with the purpose of evaluating perturbations in the shape of the Wigner ellipse. Panel (d) shows the evolution of the determinant \mathcal{S} , which is consistent with the cancellation of the effects produced by accident tiles (A).

The premise in designing the anti-accident is that its setup requires knowing in advance how the original decoherence event modifies the covariance matrix determinant, so that this modification can be cancelled. There is not a unique way to cancel the effects of a decoherence event, for simplicity we assumed that the anti-accidents in Figure 5, panel (a), share the same duration and act over the same span of frequencies as the corresponding accidents. After this simplification, α_{Γ} is the only parameter that needs to be determined to complete the configuration of a counterterm. Knowing the value of $\mathcal S$ after crossing the

original accident at the value of k where its effect is maximal, we determined the amplitude of the anti-accident by bisection, taking advantage of the fact that the numerical routine is sufficiently fast to evaluate each iteration without a significant computational cost, needing only a few iterations to converge. Some of the additional parameters in this configuration that can be tuned without producing major alterations in the final outcome are the time interval separating an accident from its anti-accident (set to zero in our case), the duration of the anti-accident (which can shift its required amplitude) or the shape of the time and frequency windows (which has to be equally changed for both the accident and the anti-accident).

The red curve in Figure 5, panel (b), shows that the shape of the power spectrum is indistinguishable from the case free of accidents. The contrast with the accident-only case (plotted with a black dotted curve) confirms that the anti-accidents (\bar{A}) restore the spectrum to its unperturbed form (which is also visible in the black dotted curve in Figure 4, panel (b)). Although not shown here, we verified that the mode evolution is modified only during the time interval in which the accident/anti-accident pair is active. Although the impact of these reversible decoherence events is not visible in the primordial power spectrum, its effects are visible for higher moments of the distribution at the level in which its dynamics is treated at nonlinear level. We leave the study of potential effects in the bispectrum for a future project.

As mentioned before, the evolution of correlators fully characterizes deformations of the Wigner ellipse through the squeezing parameters

$$\cosh(2r_k) = \frac{1}{2} \left[\frac{k^2 + \langle \tilde{\chi}'_{S}, \tilde{\chi}'_{S} \rangle + \left(\frac{L'_k}{L_k}\right)^2}{k \langle \tilde{\chi}'_{S}, \tilde{\chi}'_{S} \rangle^{1/2}} \right] , \qquad (49)$$

$$\tan(2\varphi_k) = \frac{2kL'_k L_k}{k^2 L_k^2 - (L'_k)^2 - L_k^2 \langle \tilde{\chi}'_S, \tilde{\chi}'_S \rangle},$$
 (50)

which are only different from the standard definitions by a rescaling factor of k. Using the evolution of field correlators at fixed wavenumbers, Figure 5, panels (c1) and (c2), illustrate how the squeezing parameters evolve away from their accident-free values as the k-modes pass through the accident/anti-accident pairs, and continue evolving up to the end of inflation. From both subpanels, it is clear that the most significant effects occur when the modes traverse each individual (anti-) accident within the pair. As an ancillary file attached to this paper, we include an animation showing the evolution of the Wigner ellipse and its projections over the normalized axes $k^{-1/2}\pi_k$ and $k^{1/2}v_k$, as an arbitrary k-mode traverses a decoherence

⁴ More explicitly, deviations are measured with respect to the squeezing parameters $\varphi_k^{(0)}$ and $r_k^{(0)}$, which arise from computing the evolution of correlators in the accident-free scenario, defined by $\mathcal{F}(k,\tau)=0$.

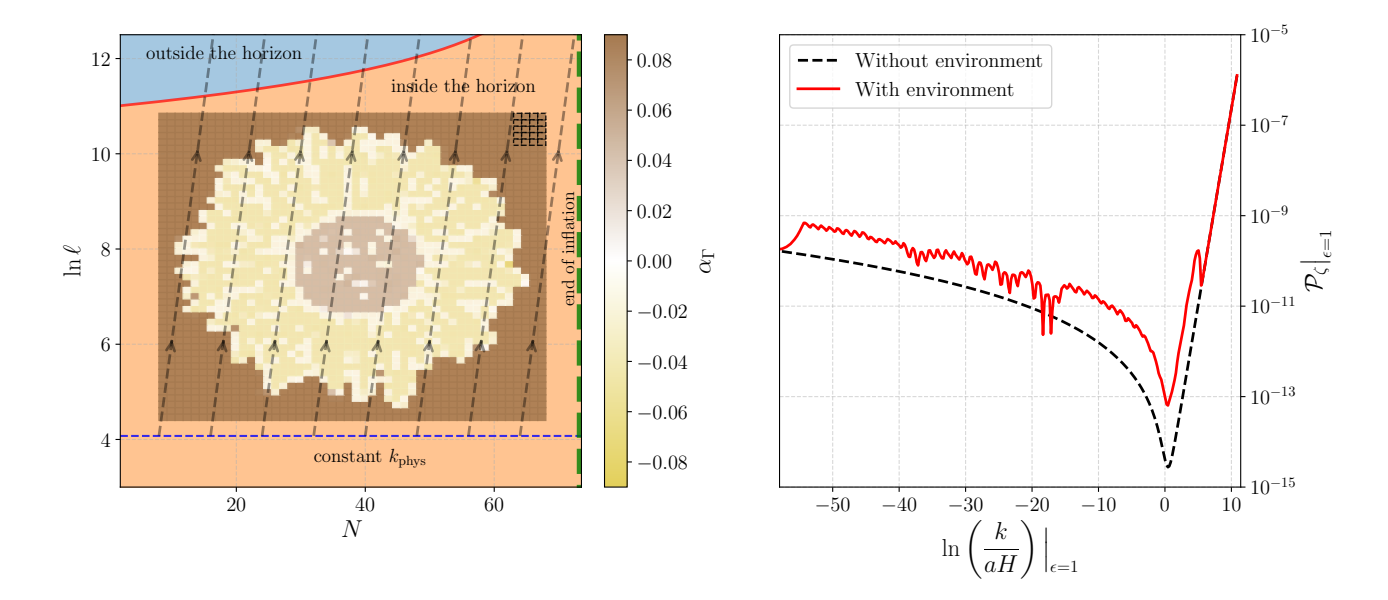


FIG. 6. Deformations in the curvature power spectrum for a large number of decoherence events. Left panel: mode injection scheme with a 48×48 array of decoherence and recoherence events forming a sunflower pattern. The small 5×4 array in the upper right corner shows the duration and the k-span for each accident in real magnitude. Using a single processor, the code resolves the dynamics of 365 modes within a few minutes, without showing signs of numerical instabilities. Right panel: resulting power spectrum of curvature fluctuations compared with the environment-free scenario. Small oscillations appear at all scales due to the presence of accidents.

event to produce a squeezed state. While arbitrary arrays of decoherence events can be used to generate squeezed states, they are more effective at inducing variations in the area of the Wigner ellipse than at producing strong squeezing.

Inset plots reveal that the variations in the phase $\Delta \varphi_k$ (visible in panel (c1), in solid light blue) track the time dependence of the source term amplitude, while the squeezing parameter Δr_k (in panel (c2), in solid blue) develops peaks that fade once the (anti-) accident is turned off. Another characteristic feature visible in the insets is the appearance of oscillations in both squeezing parameters immediately after the modes cross the accident/antiaccident pairs. These oscillations are sourced by small variations in the eccentricity of the Wigner ellipse, which induce a rotation phase that manifests as a slight "wobble". This wobble gradually fades as the modes approach horizon crossing. Such a behavior is not exclusive of the accident/anti-accident pair, since we observe that it also manifests after crossing individual accidents, regardless if α_{Γ} is positive or negative.

The evolution of the Wigner ellipse area is plotted in Figure 5, panel (d)). It demonstrates that the determinant \mathcal{S} can vary by several orders of magnitude before returning to a unit circle. For comparison, dotted lines correspond to the scenarios without anti-accidents, in which the determinant settles at a final value different from the original. This contrasts with the behavior of the squeezing parameters, whose deformations essentially vanish once the accidents are no longer active. The widths of the peaks visible in the determinant evolution depend

not only on the smoothness of the accidents, but also on the time interval separating an accident from its corresponding anti-accident.

Thus far, we have set initial conditions on a surface of constant $k_{\rm phys}$ to match the Minkowski vacuum, with the objective of studying deformations of a unit circle. In future work, we may also consider squeezed states to explore more general scenarios. This case requires careful attention, since the computational cost increases due to the rotation velocity of the ellipse, which doubles the mode-oscillation frequency and is not suppressed by the fast-frequency separation scheme introduced here. However, we have checked that the system can still be solved accurately without introducing instabilities in the determinant evolution, using the equations of motion for $\langle \tilde{\chi}_{\rm S}', \tilde{\chi}_{\rm S}' \rangle$ and L_k , given in Eqns. (40) and (41).

The numerical evolution remains stable enough to accommodate arbitrarily large arrays of tiles at minimal computational cost, allowing us to implement accidents acting at different times during mode evolution and across various k ranges. As illustrated in the left panel of Figure 6, we return to the original source-term parameterization of Eq. (33) (with squared tiles) to collocate a 48×48 array of decoherence and recoherence events arranged in a sunflower pattern. The accident distribution is loaded into the code as a bitmap, and amplitudes must be chosen carefully to avoid spurious determinant cancellations, an issue avoided by restricting $\alpha_{\Gamma} > 0$. The computational implementation permits to use either the square or the parallelogram tile configurations. Computational efficiency is achieved by updating the source term only for the deco-

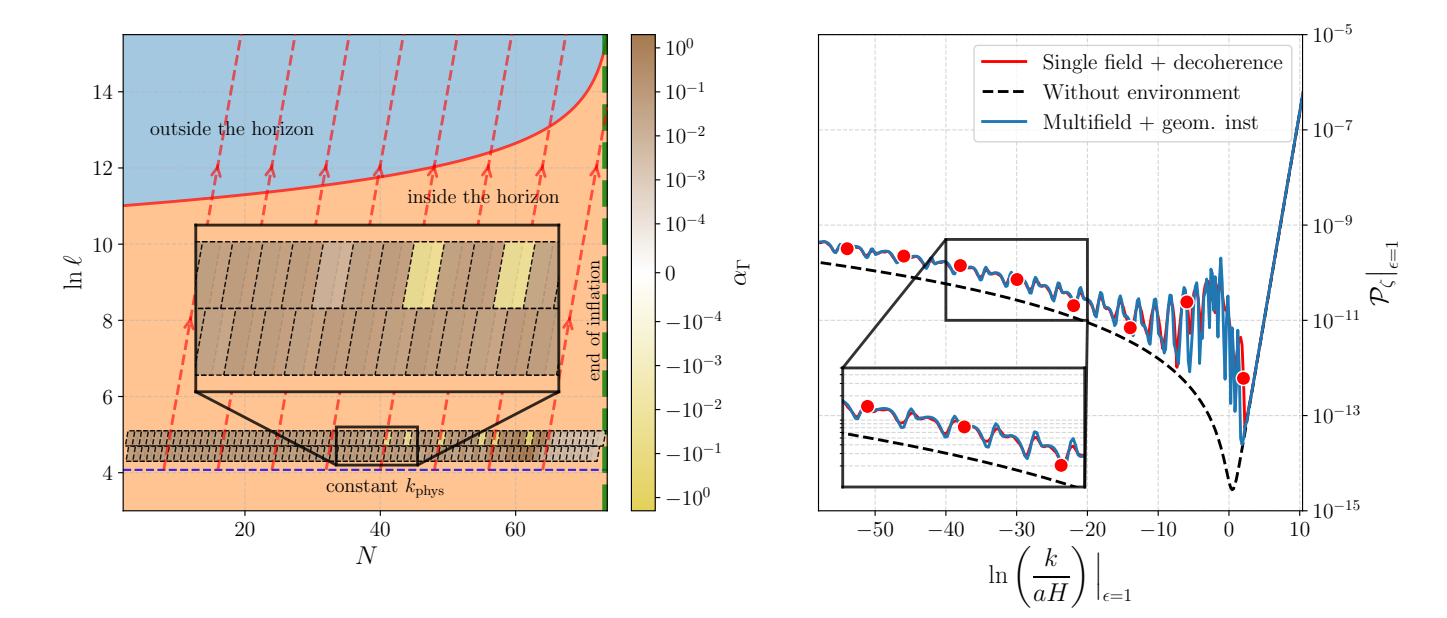


FIG. 7. Attempt to reproduce the primordial curvature power spectrum generated by a multifield model with geometrical instabilities. Left panel: Two layers of decoherence events are applied to progressively deform each k-mode. Following the same procedure as in the case of reversible decoherence accidents, the values of α_{Γ} are adjusted through a bisection method to match the power of the multifield spectrum. Right panel: Comparison of the resulting power spectra, illustrating the deformation of the single-field spectrum into the multifield one, which exhibits characteristic features induced by geometrical instabilities. The inset highlights that the discrepancies remain small but non-negligible. This reproduction strategy could be further refined by incorporating machine learning algorithms, an idea that will be explored in future work.

herence (and recoherence) tiles that contribute effectively in the evolution of each mode, making the scheme scalable. The smaller array located in the upper-right corner of the sunflower pattern illustrates the duration and wavelength coverage of individual accidents. Despite the apparent smallness of each tile, their interaction times exceed the mode-oscillation scale. These are still consistent with the timescales of the field and environment operators in which the form of the Lindblad equation in Eq. (27) is valid.

With these considerations, this setup enables the study of decoherence in close analogy with a scattering problem involving measurements of the "out" states from multiple targets. Such arrays of decoherence events can also be viewed as analogues of arbitrary pumping protocols in quantum optics, deforming the Wigner ellipse through changes in its area and degree of squeezing, and thereby inducing deformations in the curvature spectrum.

In the right panel of Figure 6, we depict the deformations of the primordial power spectrum caused by the sunflower configuration of tiles displayed in the left panel. As in Figure 4, panel (b), our results show that it is possible to produce features that may either enhance or suppress power in any band of wavenumbers. This behavior is consistent with the effective field theory approach to inflation and is particularly relevant for mimicking effects of radiatively stable models of inflation that exhibit different forms of instabilities (e.g., [16, 31, 39–41]). It should be emphasized that, although some of the power

spectra depicted in this work are not consistent with current observational constraints, their role is to exemplify the flexibility of the framework in accommodating a wide variety of feature profiles at different wavelengths.

The results shown in Figures 5 and 6 suggest that decoherence accidents can be configured to reconstruct the primordial power spectra of more intricate inflationary models. In Figure 7, we construct a sequence of decoherence events designed to reproduce the characteristic features of a multifield inflationary model mode by mode. The power spectrum of such a model exhibits multiple deformations induced by instabilities sourced by the field-space curvature. As an example, we produced the spectrum of a two-field model where the background dynamics is governed by the potential

$$V(\phi, \sigma) = \frac{\lambda}{4}\phi^4 + \frac{g}{2}\phi^2\sigma^2, \qquad (51)$$

where $\lambda = 10^{-14}$ and $g = 2\lambda$ are the model parameters. In addition to this, the background trajectories deviate from their convergence path toward the attractor due to the following field-space diagonal metric

$$h_{AB} = \delta_A^{\phi} \delta_B^{\phi} + A_{\sigma} \sin\left(\frac{\phi}{f_{\phi}}\right) \delta_A^{\sigma} \delta_B^{\sigma}, \qquad (52)$$

where chose $A_{\sigma}=0.75$ and $f_{\phi}=10^{-1}M_{\rm Pl}$ as the metric parameters. This field-space geometry causes the

background trajectories to oscillate rather than converge monotonically. Consequently, these oscillations induce time-dependent modifications to the effective oscillation frequency in the mode equations through the associated field-space curvature [16]. Using the parallelogram parameterization of tiles introduced in Eq. (48), we adopt the same quartic single-field potential used throughout this section as a baseline and modify the mode evolution through the inclusion of decoherence events. Following the same procedure used for constructing accident/antiaccident pairs, and taking the power of each k-mode of the multifield spectrum as the target, we apply a bisection method to determine the values of α_{Γ} required to reproduce the desired power. The left panel of this figure shows the pumping protocol constructed for this task, which is not unique. The inset shows a two-layer structure of overlapping tiles: the first layer of tiles provides a crude approximation to the target power value, while the second layer refines the result. The use of overlapping tiles improves the smoothness of the reconstructed spectrum.

The right panel compares the curvature spectrum obtained from this deformation procedure with both the original and target spectra. The results shown in this figure exploit an expected degeneracy: initial-state deformations in a simple inflationary scenario and dynamical features of a more intricate model can, in principle, produce (nearly) indistinguishable primordial power spectra. Although the resulting spectrum exhibits small but non-negligible deviations from the multifield spectrum, this indicates that more precise convergence techniques – such as those based on machine learning algorithms – may be required to reduce these discrepancies to machine precision. Nevertheless, our results are sufficient to demonstrate that, starting from a basic inflationary model, this formalism can reproduce features in the power spectrum characteristic of more sophisticated models using relatively simple sequences of decoherence events.

III. NUMERICAL IMPLEMENTATION OF DECOHERENCE IN MULTIFIELD INFLATION

The objective of this section is to apply the open-system formalism introduced in section II to a linearized \mathcal{N} -field system, where fields interact among themselves while the system is also coupled to an environment. We also extend the fast-slow separation scheme to solve the transport equations for the two-point correlation functions of multiple fields and their conjugate momenta. One of the main goals is to capture the cross-correlations between fields to observe how decoherence effects propagate across them. Consequently, these effects are also reflected in the evolving projections of the $2\mathcal{N}$ -dimensional Wigner ellipse.

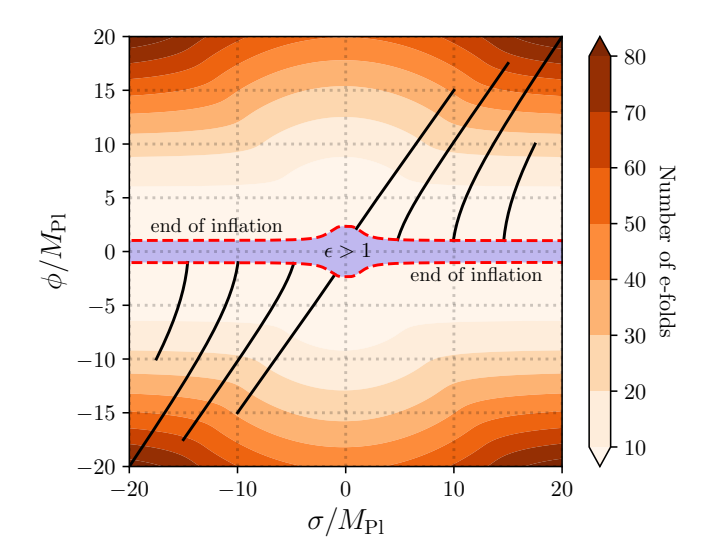


FIG. 8. Map of initial conditions that produce \mathcal{N} e-folds of inflation in the multifield potential $V(\phi,\sigma)=\frac{\lambda}{4}\phi^4+\frac{g}{2}\phi^2\sigma^2$. We selected a few background trajectories (in solid black lines) to show how these converge toward the dotted black lines that denote the end of inflation. The blue region indicates the region where the first slow-roll parameter ϵ exceeds unity, signaling the termination of the phase of exponential expansion.

A. Review of perturbation dynamics for multifield inflation

As a first step, it is essential to describe the evolution of a multifield inflationary model within the framework of first-order perturbation theory. Field dynamics is governed by the action

$$S = \int d^4x \sqrt{-g} \left(\frac{M_{\rm Pl}^2}{2} R - \frac{1}{2} \nabla_\mu \phi_A \nabla^\mu \phi^A - V(\phi_A) \right),$$
(53)

which is a straightforward generalization of the single-field action in Eq. (1). Here, capital Latin indices denote each of the \mathcal{N} scalar fields, which are raised and lowered by the field metric h_{AB} . In general, this field-space metric is a function of the background fields. As for the equations of motion for the background fields, these are also an extension of the single-field scenario

$$\ddot{\phi}_A + 3H\dot{\phi}_A + \frac{\partial V(\phi_B)}{\partial \phi_A} = 0, \qquad (54)$$

Throughout this section, we focus on the two-fields non-linear potential used by the end of the last section in Eq. (51), which serves as a test case for the transport evolution scheme of two-point correlators. In Figure 8, we show the evolution of several background trajectories, together with a map of the number of e-folds of inflation generated for different initial conditions with $\lambda = 10^{-14}$ and $q = 2\lambda$ as model parameters. All trajectories start

with sufficiently high values of the potential, with vanishing initial velocities ($\dot{\phi} = \dot{\sigma} = 0$), and evolve until the end of inflation. As in the single-field case, we identified the end of inflation by the slow-roll condition $\epsilon = 1$.

As for the dynamics of field perturbations, we adopt spatially flat spacetime coordinates, defined as a deformation of the flat FLRW metric,

$$g_{\mu\nu} = -(1+2A)\delta^t_{\mu}\delta^t_{\nu} - 2a^2B_{,i}\delta^t_{\mu}\delta^i_{\nu} + a^2\delta_{ij}\delta^i_{\mu}\delta^j_{\nu}, \quad (55)$$

where A and B are scalar metric perturbations. In these coordinates, the field perturbations $\delta \phi_A(\mathbf{x}, t)$ evolve according to the action in Eq. (53) expanded up to second order:

$$S_2 = \frac{1}{2} \int d^4 x \, a^3 \left(\delta \dot{\phi}_A \delta \dot{\phi}^A - \frac{1}{a^2} \nabla^i \delta \phi_A \nabla_i \delta \phi^A - \mathcal{M}^{AB} \delta \phi_A \delta \phi_B \right), \tag{56}$$

where we restrict to the case of a canonical kinetic term $h_{AB} = \delta_{AB}$, so the placement of indices becomes irrelevant. With a flat field space metric, the effective mass matrix \mathcal{M}^{AB} reduces to

$$\mathcal{M}^{AB} \equiv \frac{\partial^2 V}{\partial \phi^A \partial \phi^B} - \frac{1}{a^3 M_{\rm Pl}^2} \frac{\mathrm{d}}{\mathrm{d}t} \left(\frac{a^3}{H} \dot{\phi}^A \dot{\phi}^B \right) \,. \tag{57}$$

In the same way as in the treatment of perturbations in the single-field case, it is convenient to perform a Fourier mode decomposition on constant time hypersurfaces $\delta\phi^A(\mathbf{x},t)=(2\pi)^{-3/2}\int d^3\mathbf{k}~e^{i\mathbf{k}\cdot\mathbf{x}}\Phi^A_{\mathbf{k}}(t)$. In Fourier domain and in conformal time, the action for the perturbation modes reads

$$S_2 = \frac{1}{2} \int d\tau d^3 \mathbf{k} \ a^2 \left[\Phi_{\mathbf{k}}^{\prime A} \Phi_{-\mathbf{k}}^{\prime A} - a^2 \left(\frac{k^2}{a^2} \delta_{AB} - \mathcal{M}_{AB} \right) \Phi_{\mathbf{k}}^A \Phi_{-\mathbf{k}}^B \right].$$
 (58)

Furthermore, we can perform an additional variable redefinition $v_{\mathbf{k}}^A \equiv a\Phi_{\mathbf{k}}^A$ to recast the action in a form amenable

for canonical scalar field quantization

$$S_2 = \frac{1}{2} \int d\tau \ d^3 \mathbf{k} \ \left[v_{\mathbf{k}}^{\prime A} v_{-\mathbf{k}}^{\prime A} - \Omega_{AB}^2 v_{\mathbf{k}}^A v_{-\mathbf{k}}^B \right] , \qquad (59)$$

where the effective oscillation frequency matrix Ω^2 is given by

$$\Omega_{AB}^2 \equiv \left(k^2 - \frac{a''}{a}\right)\delta_{AB} + a^2 \mathcal{M}_{AB}.$$
 (60)

which makes the resulting action in Eq. (59) different from Eq. (58) only by a total conformal time derivative. With the action written in canonical form, the first step toward field quantization is to construct the system's Hamiltonian via a Legendre transformation

$$H_{\text{sys}} = \int_{\mathbb{R}^{3+}} d^3 \mathbf{k} \left[\pi_{\mathbf{k}}^A (\pi_{\mathbf{k}}^A)^{\dagger} + \Omega_{AB}^2 v_{\mathbf{k}}^A (v_{\mathbf{k}}^B)^{\dagger} \right]. \tag{61}$$

where, as in the single-field case, the integration is performed over the upper half of the Fourier sphere, which eliminates the distinction between $+\mathbf{k}$ and $-\mathbf{k}$ modes. From this point, quantization proceeds by promoting the canonical field variables to quantum operators. As in section II, the Hermiticity of the operators guarantees that the expectation values of the fields and their conjugate momenta remain real. To make this explicit, we introduce the following field redefinitions.

$$\hat{v}_{R}^{A} \equiv \frac{\hat{v}^{A} + (\hat{v}^{A})^{\dagger}}{\sqrt{2}} \quad , \quad \hat{v}_{I}^{A} \equiv \frac{\hat{v}^{A} - (\hat{v}^{A})^{\dagger}}{\sqrt{2}i},$$
 (62)

where the R and I labels refer to the "real" and "imaginary" parts of the original mode operators, and the same expressions can be extended to their corresponding conjugate momenta. With respect to these operators, the canonical commutation relations are an extension of the single-field case given by

$$\left[\hat{v}_{S}^{A}(\mathbf{k}), \hat{\pi}_{S'}^{B}(\mathbf{k}')\right] = i\delta^{AB}\delta_{SS'}\delta^{(3)}\left(\mathbf{k} - \mathbf{k}'\right), \quad (63)$$

where the indices $S, S' \in \{R, I\}$. Thus, the Hamiltonian can be recast as an Hermitian operator

$$\hat{H}_{\text{sys}} = \frac{1}{2} \sum_{S \in \{B,I\}} \int_{\mathbb{R}^{3+}} d^3 \mathbf{k} \left[\hat{\pi}_S^A (\hat{\pi}_S^A)^{\dagger} + \Omega_{AB}^2 \hat{v}_S^A (\hat{v}_S^B)^{\dagger} \right].$$
 (64)

in the same way as the field operators and their conjugate momenta. From now on, we omit the wavevector dependence for conciseness in the notation. With the Hermitian field operators in place, we can define the multifield version of a state vector

$$\hat{\mathbf{R}} = \left(\hat{v}_{\mathrm{R}}^{A}, \hat{\pi}_{\mathrm{R}}^{B}, \hat{v}_{\mathrm{I}}^{C}, \hat{\pi}_{\mathrm{I}}^{D}\right)^{\mathrm{T}}.$$
(65)

where the only purpose of the field indices is to denote that this is an $4 \times \mathcal{N}$ array. The covariance matrix elements are defined as the vacuum expectation values of the anticommutator of state vector operators

$$\langle \hat{\mathbf{\Sigma}} \rangle \equiv \left\langle \left\{ \hat{\mathbf{R}}, \hat{\mathbf{R}} \right\} \right\rangle = \langle \hat{\mathbf{\Sigma}}_{R} \rangle \oplus \left\langle \hat{\mathbf{\Sigma}}_{I} \right\rangle,$$
 (66)

where, as in the single-field case, the last equality implies

that cross-correlations between the real and imaginary parts vanish. Specifically, each of these $2\mathcal{N} \times 2\mathcal{N}$ submatrices is computed from the expectation values of the following anticommutators of the field operators

$$\left[\hat{\Sigma}_{\mathbf{S}}^{(vv)}\right]^{AB} = \left\{\hat{v}_{\mathbf{S}}^{A}, \hat{v}_{\mathbf{S}}^{B}\right\},\tag{67a}$$

$$\left[\hat{\Sigma}_{S}^{(vp)}\right]^{AB} = \left\{\hat{v}_{S}^{A}, \hat{\pi}_{S}^{B}\right\}, \tag{67b}$$

$$\left[\hat{\Sigma}_{\mathrm{S}}^{(pp)}\right]^{AB} = \left\{\hat{\pi}_{\mathrm{S}}^{A}, \hat{\pi}_{\mathrm{S}}^{B}\right\},\tag{67c}$$

which implies that the covariance submatrices in Eq. (66) – i.e., the real and imaginary parts of the full covariance matrix – can be structured as follows:

$$\langle \hat{\mathbf{\Sigma}}_{S} \rangle = \begin{bmatrix} \left\langle \hat{\Sigma}_{S}^{(vv)} \right\rangle_{AB} & \left\langle \hat{\Sigma}_{S}^{(vp)} \right\rangle_{AB} \\ \left\langle \hat{\Sigma}_{S}^{(vp)} \right\rangle_{AB}^{T} & \left\langle \hat{\Sigma}_{S}^{(pp)} \right\rangle_{AB} \end{bmatrix}. \tag{68}$$

After comparing with Eq. (15), it is clear that this is a straightforward generalization of the single-field scenario. In the Wigner formalism, these matrices encapsulate the complete information of a multifield state for a given k-mode. The time evolution for the correlators is governed by the Liouville equation

$$\frac{\mathrm{d}}{\mathrm{d}\tau} \langle \hat{\mathbf{\Sigma}}_{\mathrm{S}} \rangle = i \left\langle \left[\hat{H}_{\mathrm{sys}}, \hat{\mathbf{\Sigma}}_{\mathrm{S}} \right] \right\rangle, \tag{69}$$

and, upon substitution of the operator definitions in Eqns. (67a–67c), we find the corresponding transport equations for each of the covariance matrix components

$$\frac{\mathrm{d}}{\mathrm{d}\tau} \left\langle \hat{\Sigma}_{\mathrm{S}}^{(vv)} \right\rangle_{AB} = \mathrm{Sym}_{AB}^{CD} \left\langle \hat{\Sigma}_{\mathrm{S}}^{(vp)} \right\rangle_{CD} , \qquad (70a)$$

$$\frac{\mathrm{d}}{\mathrm{d}\tau} \left\langle \hat{\Sigma}_{\mathrm{S}}^{(vp)} \right\rangle_{AB} = \left\langle \hat{\Sigma}_{\mathrm{S}}^{(pp)} \right\rangle_{AB} - \Omega_{AC}^2 \left\langle \hat{\Sigma}_{\mathrm{S}}^{(vv)} \right\rangle_{CB} , (70b)$$

$$\frac{\mathrm{d}}{\mathrm{d}\tau} \left\langle \hat{\Sigma}_{\mathrm{S}}^{(pp)} \right\rangle_{AB} = -\mathrm{Sym}_{AB}^{CD} \left\{ \Omega_{CE}^{2} \left\langle \hat{\Sigma}_{\mathrm{S}}^{(vp)} \right\rangle_{ED} \right\}, \quad (70c)$$

where the 4-index operator (Anti)Sym (anti-)symmetrizes the target object. Extending our procedures from the single-field section even further, it is possible to combine these equations of motion into a set of third-order equations of motion

$$\left[\delta_{AC} \frac{\mathrm{d}^{3}}{\mathrm{d}\tau^{3}} + 4\Omega_{AC}^{2} \frac{\mathrm{d}}{\mathrm{d}\tau} + 2\left(\Omega_{AC}^{2}\right)'\right] \left\langle \hat{\Sigma}_{S}^{(vv)} \right\rangle_{CB} - 2 \operatorname{Antisym}_{AE}^{CD} \left\{ \left\langle \hat{\Sigma}_{S}^{(vp)} \right\rangle_{CD} \right\} \Omega_{EB}^{2} \equiv \Upsilon_{AB}, \tag{71a}$$

$$\operatorname{Sym}_{AB}^{CD} \left[\Upsilon_{CD} \right] = 0, \tag{71b}$$

where, in general, the antisymmetrized cross-correlations in the definition of the auxiliary variable Υ do not vanish in the presence of multiple fields. It is also worth noting that the definition of Υ preserves the same structure as in the single-field case. However, since it is now a matrix relation, matrix products couple the different degrees of freedom. As a result, the evolution of the correlators is no longer independent component by component, but instead encodes the transfer of information and correlations across different field modes. Not surprisingly, the appearance of this extra term suggests an alternative to mimic multifield effects within a single-field setup: by allowing the source term $\mathcal{F}(k,\tau)$ in Eq. (31) to encode the cross-correlations with external fields.

B. Transport equations and open-system dynamics for multiple fields

The previous subsection established our conventions and derived the transport equations for two-point correlators in the case of multiple interacting fields at the perturbative level. With this in mind, the objective of this subsection is to extend the open-system formalism developed in [18–21], and derive the corresponding transport equations for the case in which the multifield system develops its first nontrivial corrections through interactions with an environment. To achieve this, we consider the same Hamiltonian from Eq. (23)

$$\hat{H}_{\rm tot} = \hat{H}_{\rm sys} \otimes \hat{\mathbb{1}}_{\rm env} + \hat{\mathbb{1}}_{\rm sys} \otimes \hat{H}_{\rm env} + g\hat{H}_{\rm int},$$
 (72)

where the system Hamiltonian H_{sys} , given in Eq. (64), is a sum of quadratic interacting actions. This structure ensures that the dynamics of different k-modes are independent, while, for a given k-mode, perturbations from the various field components remain coupled. The environment Hamiltonian \hat{H}_{env} is chosen such that (a) all of the environment operators (including the density matrix in the interaction picture) remain nearly stationary, and (b) it is approximately time-independent. Finally, the interaction Hamiltonian \hat{H}_{int} is separable into system and environment operators, and thus retains the same form as in Eq. (24). Therefore, considering that the derivation developed in [34] does not constrain the number of interacting fields in the systems' Hamiltonian, the evolution of the submatrices of covariance correlators described in Eq. (68) is determined by the following Lindblad equation

$$\frac{\mathrm{d}}{\mathrm{d}\tau}\langle\hat{\mathbf{\Sigma}}_{\mathrm{S}}\rangle = -i\left\langle \left[\hat{\mathbf{\Sigma}}_{\mathrm{S}}, \hat{H}_{\mathrm{sys}}\right]\right\rangle - (2\pi^{3})^{1/2}\Gamma \int_{\mathbb{R}^{3+}} d^{3}\mathbf{k} \ \tilde{C}_{E}(\mathbf{k}, \tau) \left\langle \left[\left[\hat{\mathbf{\Sigma}}_{\mathrm{S}}, \hat{I}_{\mathbf{k}}^{\mathrm{S}}\right], \hat{I}_{\mathbf{k}}^{\mathrm{S}}\right]\right\rangle, \tag{73}$$

where the coupling constant $\Gamma \equiv 2g^2\tau_c$ is fixed under the assumption that the field interaction timescales (with τ_c scaling approximately as the inverse square root of the eigenvalues of Ω^2) are much shorter than the characteristic timescales of the environment.

The operator $\hat{I}_{\mathbf{k}}^{\mathbf{S}}$ is limited to act over system states, and in the same way as in the single-field scenario, the first nontrivial corrections from the extra terms in the Lindblad equation arise by considering that such an operator is a

linear combination of the field and momentum operators

$$\hat{I}_{\mathbf{k}}^{\mathbf{S}} = \alpha_A(\tau)\hat{v}_{\mathbf{S}}^A + \beta_B(\tau)\hat{\pi}_{\mathbf{S}}^B, \qquad (74)$$

where there is no difference if we pick either the real or the imaginary parts of the field, since the dynamical results are the same given our choice of covariance operators. Fixing $\hat{I}_{\mathbf{k}}^{\mathrm{S}} = \alpha_A(\tau)\hat{v}_{\mathrm{S}}^A$, the evolution equations for the covariance matrix components are found by substituting the definitions from Eqns. (67a–67c) and the system Hamiltonian from Eq. (64) in the Lindblad equation

$$\frac{\mathrm{d}}{\mathrm{d}\tau} \left\langle \hat{\Sigma}_{\mathrm{S}}^{(vv)} \right\rangle_{AB} = \mathrm{Sym}_{AB}^{CD} \left\langle \hat{\Sigma}_{\mathrm{S}}^{(vp)} \right\rangle_{CD} , \tag{75a}$$

$$\frac{\mathrm{d}}{\mathrm{d}\tau} \left\langle \hat{\Sigma}_{\mathrm{S}}^{(vp)} \right\rangle_{AB} = \left\langle \hat{\Sigma}_{\mathrm{S}}^{(pp)} \right\rangle_{AB} - \Omega_{AC}^2 \left\langle \hat{\Sigma}_{\mathrm{S}}^{(vv)} \right\rangle_{CB}, \tag{75b}$$

$$\frac{\mathrm{d}}{\mathrm{d}\tau} \left\langle \hat{\Sigma}_{\mathrm{S}}^{(pp)} \right\rangle_{AB} = -\mathrm{Sym}_{AB}^{CD} \left\{ \Omega_{CE}^{2} \left\langle \hat{\Sigma}_{\mathrm{S}}^{(vp)} \right\rangle_{ED} \right\} + 2\mathcal{F}_{AB} , \qquad (75c)$$

where $\mathcal{F}_{AB} \equiv (2\pi)^{3/2}\Gamma \tilde{C}_E \alpha_A \alpha_B = \mathcal{F}(k,\tau)\alpha_A \alpha_B$. Here the last equality implies that it is possible to reuse the tile parameterizations proposed in the single-field case in Eqns. (33) or (48). To solve for the case of a general linear combination in Eq. (74), we find that the corresponding transport equations have the same form as in Eqns. (75a–75c) provided that the following variable redefinitions are applied

$$\left\langle \hat{\Sigma}_{S}^{(vv)} \right\rangle_{AB} \longrightarrow \overline{\left\langle \hat{\Sigma}_{S}^{(vv)} \right\rangle}_{AB} = \left\langle \hat{\Sigma}_{S}^{(vv)} \right\rangle_{AB},$$
 (76a)

$$\left\langle \hat{\Sigma}_{S}^{(vp)} \right\rangle_{AB} \longrightarrow \overline{\left\langle \hat{\Sigma}_{S}^{(vp)} \right\rangle}_{AB} = \left\langle \hat{\Sigma}_{S}^{(vp)} \right\rangle_{AB} + (2\pi)^{3/2} \Gamma \tilde{C}_{E} \beta_{A} \beta_{B} ,$$
 (76b)

$$\left\langle \hat{\Sigma}_{\mathrm{S}}^{(pp)} \right\rangle_{AB} \longrightarrow \overline{\left\langle \hat{\Sigma}_{\mathrm{S}}^{(pp)} \right\rangle_{AB}} = \left\langle \hat{\Sigma}_{\mathrm{S}}^{(pp)} \right\rangle_{AB} - (2\pi)^{3/2} \left\{ \Gamma \tilde{C}_E \operatorname{Sym}_{AB}^{CD} \left[\alpha_C \beta_D \right] + \left[\Gamma \tilde{C}_E \beta_A \beta_B \right]' \right\}, \tag{76c}$$

$$\mathcal{F}_{AB} \longrightarrow \overline{\mathcal{F}}_{AB} = \mathcal{F}_{AB} + (2\pi^3)^{1/2} \left\{ \Gamma \tilde{C}_E \operatorname{Sym}_{AB}^{CD} \left[\Omega_{ED}^2 \beta_C \beta_E \right] - \left[\Gamma \tilde{C}_E \operatorname{Sym}_{AB}^{CD} \left(\alpha_C \beta_D \right) \right]' + \left[\Gamma \tilde{C}_E \beta_A \beta_B \right]'' \right\}, \quad (76d)$$

where primes denote derivatives with respect to conformal time. Since these expressions generalize our results in the single-field case presented in Eqns. (30a-30d), it is possible to solve the same transport equations in Eqns. (75a-75c) and invert these variable redefinitions on the solutions to find the results for other forms of coupling with the environment.

The set of equations in Eqns. (75a–75c) forms a coupled system of equations of motion for the evolution of the covariance matrix under decoherence effects, which are similar to what was derived in [21, 34]. As in the case free of environmental effects, we may attempt to condense these equations into a single set of third-order differential equations for the mode correlators

$$\operatorname{Sym}_{AB}^{CD} \left[\Upsilon_{CD} \right] = 8 \mathcal{F}_{AB} \,, \tag{77}$$

where, for notational simplicity, overlines have been omitted and the auxiliary variable Υ is defined as in Eq. (71a). As in the case of a single field, the term \mathcal{F}_{AB} originates from the double commutator term in the Lindblad equation, and acts as a source term evolving independently from the mode correlators. Nevertheless, since the result still depends on the cross-correlations between the field modes and their conjugate momenta, these cross-correlations must be determined separately.

The structure of the interaction operator in Eq. (74) suggests that decoherence events can modify the dynamics of mode correlators through couplings to any of the fields. In particular, we can examine the effects of decoherence interactions along the adiabatic (\parallel) or in the isocurvature (\perp) directions, defined as

$$(\hat{v}_{\mathbf{S}}^{A})_{\parallel} \equiv \frac{\dot{\phi}^{A} \dot{\phi}_{C}}{|\dot{\phi}|^{2}} \hat{v}_{\mathbf{S}}^{C}, \qquad (78a)$$

$$(\hat{v}_{S}^{A})_{\perp} \equiv \left[\delta_{C}^{A} - \frac{\dot{\phi}^{A}\dot{\phi}_{C}}{|\dot{\phi}|^{2}}\right]\hat{v}_{S}^{C}, \qquad (78b)$$

where $|\dot{\phi}|^2$ denotes the norm squared of the background velocities in a flat field-space geometry. Since the same projection-based definitions extend naturally to the corresponding conjugate momenta, the interaction operator $\hat{I}_{\mathbf{k}}^{\mathrm{S}}$ can also be projected along either direction. For example,

its projection onto the parallel direction is

$$\hat{I}_{\parallel}^{S} = \alpha_{A}(\tau)(\hat{v}_{S}^{A})_{\parallel} + \beta_{B}(\tau)(\hat{\pi}_{S}^{B})_{\parallel}, \qquad (79)$$

$$= \left(\alpha_{A}(\tau)\frac{\dot{\phi}^{A}\dot{\phi}_{C}}{|\dot{\phi}|^{2}}\right)\hat{v}_{S}^{C} + \left(\beta_{B}(\tau)\frac{\dot{\phi}^{B}\dot{\phi}_{D}}{|\dot{\phi}|^{2}}\right)\hat{\pi}_{S}^{D},$$

$$= \tilde{\alpha}_{C}(\tau)\hat{v}_{S}^{C} + \tilde{\beta}_{D}(\tau)\hat{\pi}_{S}^{D},$$

where $\tilde{\alpha}_C(\tau) \equiv \alpha_A(\tau)\dot{\phi}^A\dot{\phi}_C/|\dot{\phi}|^2$ and $\tilde{\beta}_D(\tau) \equiv \beta_B(\tau)\dot{\phi}^B\dot{\phi}_D/|\dot{\phi}|^2$ specify the transformed time-dependent coefficients in the linear combination. This shows that the variable redefinitions described in Eqns. (76a–76d) are sufficient to find the mode correlators for the case of an adiabatic interaction operator. The same reasoning applies to the operator projected along the isocurvature direction, or to any other combination of both directions.

C. Implementation of a dynamical coloring scheme via Cholesky decomposition

Up to this point, we have established that Eqns. (75a-75c) govern the evolution of the following mode correlators

$$\left\langle \hat{\Sigma}_{\mathrm{S}}^{(vv)} \right\rangle^{AB} = 2 \left\langle \hat{v}_{\mathrm{S}}^{A}, \hat{v}_{\mathrm{S}}^{B} \right\rangle,$$
 (80a)

$$\left\langle \hat{\Sigma}_{S}^{(vp)} \right\rangle^{AB} = \left\langle \hat{v}_{S}^{A}, \hat{\pi}_{S}^{B} \right\rangle + \left\langle \hat{\pi}_{S}^{B}, \hat{v}_{S}^{A} \right\rangle,$$
 (80b)

$$\left\langle \hat{\Sigma}_{\mathrm{S}}^{(pp)} \right\rangle^{AB} = 2 \left\langle \hat{\pi}_{\mathrm{S}}^{A}, \hat{\pi}_{\mathrm{S}}^{B} \right\rangle ,$$
 (80c)

which describe the evolution of a Gaussian state subject to an arbitrary sequence of decoherence events. The objective of this subsection is to introduce a fast-slow decomposition scheme analogous to the amplitude-phase separation procedure discussed in subsection II C. To this end, based on the approach developed in [27], we decompose the field and momentum variables in the same way as in the single field-case

$$\hat{v}_{\rm S}^A \to L_{AB} \tilde{\chi}_B \,, \tag{81a}$$

$$\hat{\pi}_{\rm S}^A \to L'_{AB} \tilde{\chi}_B + L_{AB} \tilde{\chi}'_B \,.$$
 (81b)

Here L_{AB} denotes the elements of a real matrix encoding the field amplitude, and $\tilde{\chi}_A$ denotes an element from a set of \mathcal{N} time-dependent Gaussian random variables. In line with the Wigner formalism, Gaussian random variables are sufficient to reproduce a large number of field realizations consistent with a Gaussian state [42]. Statistical averages are therefore computed with respect to $\tilde{\chi}$ only. In terms of these variables, the mode correlator $\langle \hat{v}_{\rm S}^A, \hat{v}_{\rm S}^B \rangle$ can be expressed as

$$\langle \hat{v}_{S}^{A}, \hat{v}_{S}^{B} \rangle = L_{AC} L_{BD} \langle \tilde{\chi}_{C}, \tilde{\chi}_{D} \rangle$$

$$= L_{AC} L_{CB}^{T},$$
(82)

where we impose the normalization condition

$$\langle \tilde{\chi}_C, \tilde{\chi}_D \rangle = \delta_{CD} \,, \tag{83}$$

which fixes the variance to unity at all times. This matrix factorization defines a coloring transformation [43], in which the stochastic variables $\tilde{\chi}$ capture the statistical properties of the Gaussian state, while the matrices L and L' encode its deterministic evolution. As a direct by-product of introducing the fast–slow decomposition, the original transport problem can be reintepreted as a dynamical coloring problem. In this formulation, deriving the equations of motion for the coloring factors (i.e., the matrix L) from Eqns. (75a–75c) provides a direct description of how the coloring transformation evolves in time.

As a first step toward obtaining dynamical coloring transformations, we rewrite the mode correlators from Eqns. (80a–80c) in terms of the coloring matrix L_{AB} and the velocity correlators between the Gaussian variables and their derivatives

$$\left\langle \hat{\Sigma}_{S}^{(vv)} \right\rangle_{AB} = 2L_{AC}L_{CB}^{T}, \qquad (84a)$$

$$\left\langle \hat{\Sigma}_{S}^{(vp)} \right\rangle_{AB} = 2L_{AC}\left(L_{CB}^{T}\right)' + 2L_{BD}\langle \tilde{\chi}_{D}', \tilde{\chi}_{C} \rangle L_{CA}^{T}, \qquad (84b)$$

$$\left\langle \hat{\Sigma}_{S}^{(pp)} \right\rangle_{AB} = 2\left(L_{AC}\right)'\left(L_{CB}^{T}\right)' + 2L_{BD}\langle \tilde{\chi}_{D}', \tilde{\chi}_{C} \rangle \left(L_{CA}^{T}\right)' + 2L_{AC}\langle \tilde{\chi}_{C}', \tilde{\chi}_{D} \rangle \left(L_{DB}^{T}\right)' + 2L_{AC}\langle \tilde{\chi}_{C}', \tilde{\chi}_{D} \rangle L_{DB}^{T}, \qquad (84c)$$

where, since the analysis is restricted to Gaussian states, all statistical averages are computed through Gaussian integrals, for which the ordering of the variables is immaterial. The Hermiticity of the field operators then guarantees that the associated stochastic variables can be taken as real-valued, allowing us to represent the operators by real Gaussian variables and safely omit the commutation relations between $\tilde{\chi}$ and $\tilde{\chi}'$. As anticipated, the substitution of Eqns. (84a–84c) in the system of transport equations in Eqns. (75a–75c) yields the equations of motion for the dynamical coloring transformations. The substitution of Eqns. (84a–84b) in Eqns. (75a–75b) results in the following constraint on the $\langle \tilde{\chi}'_A, \tilde{\chi}_B \rangle$ correlators:

$$\operatorname{Sym}_{AB}^{CD}\left[\langle \tilde{\chi}_C', \tilde{\chi}_D \rangle \right] = 0, \qquad (85)$$

which corresponds to the first derivative of the variance-fixing conditions in Eq. (83), and implies that the correlator $\langle \tilde{\chi}'_A, \tilde{\chi}_B \rangle$ is antisymmetric (not zero, as in the single-field case) with respect to the indices A and B. This agrees with the intuition of the $\langle \tilde{\chi}'_A, \tilde{\chi}_B \rangle$ correlators as rotation generators of the normalized stochastic vector $\tilde{\chi}$. Combined with the derivative of this condition

$$\operatorname{Sym}_{AB}^{CD} \left[\langle \tilde{\chi}_C'', \tilde{\chi}_D \rangle + \langle \tilde{\chi}_C', \tilde{\chi}_D' \rangle \right] = 0, \qquad (86)$$

it ensures that the Gaussian random variables are independent, and fixes their variance to one at all times. In fact, the condition in Eq. (83) can also be recovered by inserting the mode correlator definitions in Eqns. (84a–84c) directly in the transport equations (Eqns. (75a–75c)). The constraints in Eqns. (85) and (86) reveal that the

derivatives of the random variable correlators are related in such a way that the system can be order-reduced. This feature is particularly advantageous when deriving the evolution equations for the coloring matrices and auxiliary correlators. Adding Eq. (75b) and its transpose, and considering again the mode correlators definitions, we find the following expression for the \boldsymbol{L} matrices

$$\operatorname{Sym}_{AB}^{CD} \left[\left(L^{-1} \right)_{CE} L_{ED}^{"} - \langle \tilde{\chi}_{C}^{"}, \tilde{\chi}_{D}^{"} \rangle + \left(L^{-1} \right)_{CE} \Omega_{EF}^{2} L_{FD} + 2(L^{-1})_{CE} L_{EF}^{"} \langle \tilde{\chi}_{F}^{"}, \tilde{\chi}_{D} \rangle \right] = 0,$$
 (87)

where the term inside the symmetrizer permits the addition of an antisymmetric matrix without altering the expression. The inclusion of an antisymmetric matrix fixes the shape of the coloring matrix, and in this specific case we add the matrix \mathcal{A}_{CD} to suppress the upper-diagonal elements of L (D > C):

$$\mathcal{A}_{CD} = -\left(L^{-1}\right)_{CE} \Omega_{EF}^2 L_{FD} + \langle \tilde{\chi}_C', \tilde{\chi}_D' \rangle -2(L^{-1})_{CE} (L_{EF})' \langle \tilde{\chi}_F', \tilde{\chi}_D \rangle,$$
(88)

which fixed the coloring factor L to be a lower-triangular Cholesky matrix with $\mathcal{N}(\mathcal{N}+1)/2$ entries at all times. Therefore, with this rearrangement of degrees of freedom, the coloring transformation defined in Eq. (83) is based on a Cholesky decomposition, which is unique in the case in which $\left\langle \hat{\Sigma}_{\mathrm{S}}^{(vv)} \right\rangle_{AB}$ is a positive-definite matrix. Thus, the equation of motion for the coloring Cholesky factor has the form

$$L''_{AB} + 2L'_{AC}\langle \tilde{\chi}'_C, \tilde{\chi}_B \rangle + L_{AC}(\mathcal{A}_{CB} - \langle \tilde{\chi}'_C, \tilde{\chi}'_B \rangle) + \Omega^2_{AC}L_{CB} = 0,$$
(89)

where the choice of \mathcal{A} guarantees that the lower-triangular shape of \mathcal{L} is preserved at all times. In what remains of this section, we will develop the case of a Cholesky decomposition but this method can be extended to other coloring transformations, as we will show in Appendix A. From the last equation, it becomes evident that the equations of motion for the random variable correlators $\langle \tilde{\chi}_B', \tilde{\chi}_C \rangle$ and $\langle \tilde{\chi}_B', \tilde{\chi}_C' \rangle$ are required to close the dynamical system for the coloring transformation. Consequently, just as in the case for the coloring matrices, we can obtain their corresponding evolution equations from the transport system equations. Rewriting Eq. (75b) and reducing the order of the Cholesky factors using Eq. (89) we derive the equations governing the dynamics of $\langle \tilde{\chi}_B', \tilde{\chi}_C \rangle$

$$\frac{\mathrm{d}}{\mathrm{d}\tau} \langle \tilde{\chi}_B', \tilde{\chi}_C \rangle = \mathcal{A}_{BC} \,, \tag{90}$$

which conserves the antisymmetric form of such correlators anticipated in Eq. (85). As for the evolution of the velocity correlators, their equations of motion can be obtained from Eq. (75c):

$$\frac{\mathrm{d}}{\mathrm{d}\tau} \langle \tilde{\chi}'_A, \tilde{\chi}'_B \rangle = \mathrm{Sym}_{AB}^{CD} \left[-2L_{CE}^{-1} L'_{EF} \langle \tilde{\chi}'_F, \tilde{\chi}'_D \rangle \right. \\
\left. -2L_{CE}^{-1} L'_{EF} \langle \tilde{\chi}'_F, \tilde{\chi}_G \rangle \langle \tilde{\chi}'_G, \tilde{\chi}_D \rangle \right. \\
\left. + \langle \tilde{\chi}'_C, \tilde{\chi}'_F \rangle \langle \tilde{\chi}'_F, \tilde{\chi}_D \rangle - \mathcal{A}_{CE} \langle \tilde{\chi}'_E, \tilde{\chi}_D \rangle \right. \\
\left. + \frac{1}{2} L_{CE}^{-1} \mathcal{F}_{EF} (L^{-1})_{FD}^{\mathrm{T}} \right], \tag{91}$$

which provides equations of motion for all of the variables in the dynamical system.

Conservation of the covariance matrix determinant plays a crucial role in verifying whether the dynamical system undergoes stable numerical evolution. In terms of the covariance block matrices, this determinant can be written as

$$S = \det \left\{ \langle \hat{\Sigma}_{S}^{(vv)} \rangle \right\} \det \left\{ \langle \hat{\Sigma}_{S}^{(pp)} \rangle - \langle \hat{\Sigma}_{S}^{(vp)} \rangle^{T} \langle \hat{\Sigma}_{S}^{(vv)} \rangle^{-1} \langle \hat{\Sigma}_{S}^{(vp)} \rangle \right\}, \tag{92}$$

where, as in the single-field scenario, it is indistinct to choose either the real (S = R) or the imaginary mode operators (S = I) since these are independent parts of the covariance matrix $\langle \hat{\Sigma} \rangle$. With respect to the coloring matrices, the determinant of each submatrix reduces to

$$S = 4^{\mathcal{N}} \det \left\{ \mathbf{L} \mathbf{L}^{T} \right\} \det \left\{ \mathbf{L} \mathbf{Z} \mathbf{L}^{T} \right\}, \qquad (93)$$

where the matrix \mathcal{Z}_{AB} is defined as

$$\mathcal{Z}_{AB} \equiv \langle \tilde{\chi}_A', \tilde{\chi}_B' \rangle + \langle \tilde{\chi}_A', \tilde{\chi}_C \rangle \langle \tilde{\chi}_C', \tilde{\chi}_B \rangle, \qquad (94)$$

which serves as an auxiliary variable introduced to isolate the contributions associated to the amplitudes from those arising from the dynamics of the random variable correlators. The role of this new variable is reminiscent to the purpose of the velocity correlator $\langle \tilde{\chi}'_{\rm S}, \tilde{\chi}'_{\rm S} \rangle$ in Eq. (47) for the single-field case. Importantly, \mathcal{Z} is the only variable other than the Cholesky factors that enters explicitly in the calculation of the determinant, making it particularly convenient for testing the conservation of \mathcal{S} . Thus, the equations of motion in Eq. (91) need to be replaced by evolution equations for the new variable

$$\frac{\mathrm{d}}{\mathrm{d}\tau} \mathcal{Z}_{AB} = \mathrm{Sym}_{AB}^{CD} \left[-2L_{CE}^{-1}L_{EF}' \mathcal{Z}_{FD} - \langle \tilde{\chi}_C', \tilde{\chi}_E \rangle \mathcal{Z}_{ED} + \frac{1}{2}L_{CE}^{-1} \mathcal{F}_{EF} \left(L^{-1} \right)_{FD}^{\mathrm{T}} \right].$$
(95)

which are the only equations affected explicitly by the presence of the environment. Hence, together with Eqns. (90) and (95), the dynamics of the coloring transformations is governed by the following equations of motion

$$L_{AB}'' + 2L_{AC}'\langle \tilde{\chi}_C', \tilde{\chi}_B \rangle + L_{AC} \left[\mathcal{A}_{CB} - \mathcal{Z}_{CB} + \langle \tilde{\chi}_C', \tilde{\chi}_D \rangle \langle \tilde{\chi}_D', \tilde{\chi}_B \rangle \right] + \Omega_{AC}^2 L_{CB} = 0,$$

$$(96)$$

where, for consistency, the definition of the shape-fixing antisymmetric matrix \mathcal{A}_{BC} in (97) also needs to be recast in terms the auxiliary variable \mathcal{Z}_{BC} :

$$\mathcal{A}_{BC} = -\left(L^{-1}\right)_{BE} \Omega_{EF}^2 L_{FC} + \mathcal{Z}_{BC} - \langle \tilde{\chi}_B', \tilde{\chi}_D \rangle \langle \tilde{\chi}_D', \tilde{\chi}_C \rangle - 2(L^{-1})_{BE} (L_{EF})' \langle \tilde{\chi}_F', \tilde{\chi}_C \rangle,$$
(97)

where (C>B). Eq. (96) constitutes a system of $\mathcal{N}(\mathcal{N}+1)/2$ equations for the entries of the lower-triangular Cholesky factors⁵. As a sanity check, it is necessary to count the number of degrees of freedom: there are $\mathcal{N}(\mathcal{N}-1)/2$ evolving constraints in Eq. (90) associated with the antisymmetric correlators $\langle \tilde{\chi}'_A, \tilde{\chi}_B \rangle$, which guarantee the preservation of the unit-variance gauge condition in Eq. (83) and the shape of the Cholesky factors. As a result of this, subtracting the number of constraints from the amount of evolving matrix elements in the coloring scheme, we find \mathcal{N} evolving degrees of freedom per k-mode, matching the number of fields.

In addition to the dynamical coloring scheme interpretation discussed above, this evolution scheme can also be understood as a fast and slow separation of degrees of freedom, since the net oscillation frequency in Eq. (96) is suppressed by the counterterm $\langle \tilde{\chi}'_A, \tilde{\chi}'_B \rangle$ in a manner analogous to our results in [27], figure 8, and to the scale separation scheme discussed in subsection II C for the single-field scenario. This suppression enables an increase of one or two orders of magnitude in the evolution time step relative to a standard mode evolution approach, allowing us to efficiently resolve the dynamics of the mode correlators undergoing decoherence events deep inside the horizon.

Some care must be taken when applying this implementation, since the original set of transport equations in Eqns. (75a–75c) still forms a third-order system with respect to $\langle \hat{\Sigma}_{\rm S}^{(vv)} \rangle$, which – when written as in Eqns. (71b) and (77) – cannot be order-reduced. At super-horizon scales, this system exhibits a sign flip in the diagonal elements of \mathcal{Z} – which are positive, by definition – leading to numerical instabilities that manifest particularly in scenarios where the background trajectories undergo sharp turns. Despite this, the framework retains enough flexibility to generate arbitrarily large features in the primordial power spectrum, provided that (a) the model potentials remain sufficiently smooth and (b) decoherence and recoherence events occur at subhorizon scales (as developed in section II for one field). Moreover, since part

of the purpose of this approach is to mimic Gaussian state deformations of more complicated dynamical setups using smooth, well-behaved models as a starting point, these conundrums do not pose severe limitations to achieving this objective. Extending this approach to accommodate potentials that induce more intricate deformations of the background evolution will be the subject of future work.

The dynamical setup requires initial conditions to be complete. As developed in section II for the single-field case, it is natural to impose instantaneous minimal variance/energy initial conditions on a hypersurface of constant $k_{\rm phys}$ prior to the onset of decoherence events. This prescription requires diagonalizing the effective oscillation frequency matrix Ω^2 at initial time $\tau=\tau_0$ in order to determine the initial mode correlators

$$\omega_{AB}|_{\tau=\tau_0} \equiv U_{AC}\Omega_{CD}^2|_{\tau=\tau_0}U_{CB}^{\mathrm{T}}, \qquad (98)$$

where ω_{AB} in the diagonal form of Ω^2 , and U is the orthonormal matrix that diagonalizes Ω^2 at $\tau = \tau_0$. It is known that this choice of instantaneous minimal energy/variance initial states is equivalent to the Minkowski vacuum. From a geometric perspective, this choice restricts the problem to the study of a multidimensional Wigner ellipse, which starts as a circle and is later deformed through an arbitrary sequence of decoherence events. Thus, the initial mode correlators are given by

$$\left\langle \hat{\Sigma}_{S}^{(vv)} \right\rangle_{AB} \Big|_{\tau=\tau_{0}} = U_{AC}^{T} \left(\frac{1}{\omega_{CD}^{1/2}} \right) U_{DB},$$
 (99a)

$$\left\langle \hat{\Sigma}_{S}^{(vp)} \right\rangle_{AB} \Big|_{\tau=\tau_0} = 0,$$
 (99b)

$$\left\langle \hat{\Sigma}_{S}^{(pp)} \right\rangle_{AB} \bigg|_{\tau=\tau_{0}} = U_{AC}^{T} \omega_{CD}^{1/2} U_{DB} .$$
 (99c)

Here, $\omega^{1/2}$ denotes the square root of each the diagonal matrix elements of ω . Although the initial conditions for the (vp) mode correlators are set to zero, they are sourced to not vanish during the evolution.

Once the initial mode correlators are set, the corresponding initial values for the dynamical coloring transformations follow directly. The initial coloring matrix is computed by performing a Cholesky decomposition of the mode correlator in Eq. (99a), while the remaining dynamical variables are determined from Eqns. (99a–99c)

 $^{^5}$ It is in distinct to fix the shape of the coloring Cholesky factors to be lower or upper-triangular matrices.

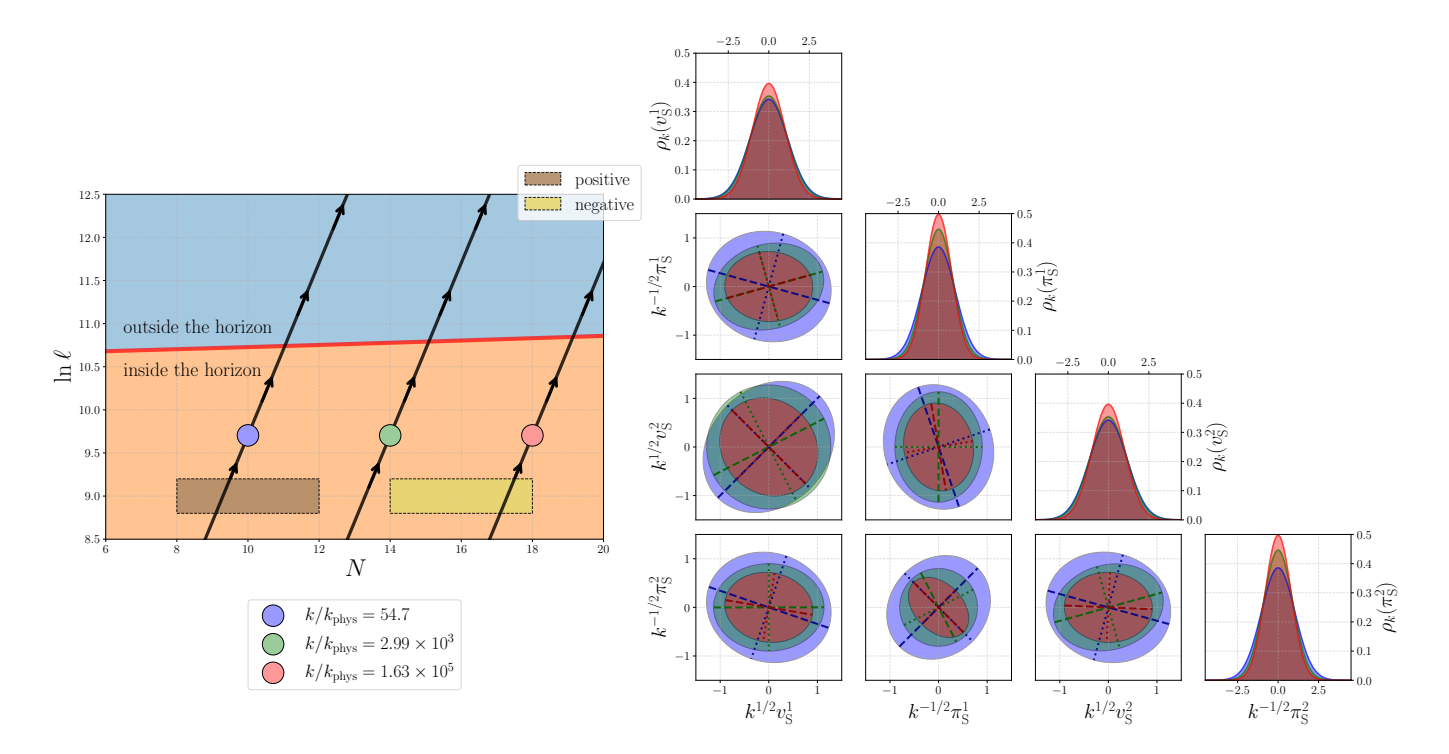


FIG. 9. Wigner ellipse evolution through decoherence and recoherence events. Left panel: Injection scheme and configuration of decoherence events with $\alpha_{\Gamma} > 0$ in brown and $\alpha_{\Gamma} < 0$ in yellow. Even in the accident-free scenario, different modes exhibit slight dephasing at subhorizon scales; however, the main source of Wigner ellipse deformations – and hence of state modifications – is the occurrence of decoherence or recoherence events, which produce distinguishable signatures. Right panel: Triangular plot showing each projection of the joint Wigner function after each decoherence event, highlighting the change in area with respect to the ellipse in the environment-free case (in green). We observe that the states deformed by decoherence (or decoherence) are slightly more squeezed than in the case free of accidents. On the rightmost side, we illustrate the deformations of the marginalized probability distributions $\rho_k(v_{\rm S}^A, \pi_{\rm S}^B)$. In addition to this plot, we generated an animation representing the evolution of the joint distribution, which is included as an ancillary file.

$$L_{AC}L_{CB}^{\mathrm{T}}\Big|_{\tau=\tau_0} = \left\langle \hat{\Sigma}_{\mathrm{S}}^{(vv)} \right\rangle_{AB}\Big|_{\tau=\tau_0},$$
 (100a)

$$L'_{AB}|_{\tau=\tau_0} = \langle \tilde{\chi}'_A, \tilde{\chi}_B \rangle|_{\tau=\tau_0} = 0, \qquad (100b)$$

$$\mathcal{Z}_{AB}|_{\tau=\tau_0} = \langle \tilde{\chi}_A', \tilde{\chi}_B' \rangle|_{\tau=\tau_0}$$

$$= \frac{1}{2} \left(L^{-1} \right)_{AE} \left\langle \hat{\Sigma}_{S}^{(pp)} \right\rangle_{EF} \bigg|_{\tau = \tau_{0}} \left(L^{-1} \right)_{FB}^{T} . \tag{100c}$$

These initial conditions complete the specification of the initial state and, when combined with the evolution equations in Eqns. (90), (95), and (96), provide a full definition of the dynamical coloring transformations. Moreover, we can apply the mode correlator redefinitions in Eqns. (76a–76d) to transform the results, and study alternative time-dependent linear combinations of field and momenta constituting the interaction operator $\hat{I}_{\mathbf{k}}^{\mathbf{S}}$ described in subsection III B.

With the complete evolution system in hand, the next subsection showcases only a small portion of the wide array of analyses enabled by our numerical implementation. Based on the dynamical coloring–transformation framework, this implementation lets us probe the first

nontrivial corrections arising from the Lindblad equation in Eq. (73) for a multifield system interacting with an environment.

D. Results: evolution of the Wigner ellipse and generation of features in the power spectrum

In addition to the deformation of initial states to reproduce the primordial spectrum of more complex (i.e., with more fields, intricate potentials, nontrivial effects from field geometry or combinations of all of these) inflationary models, the inclusion of decoherence within the multifield framework raises a fundamental question: how do these field effects manifest and propagate across coupled degrees of freedom? Addressing this question requires characterizing the dynamics of each Wigner ellipse as it undergoes the simplest sequences of decoherence events. To this end, we adopt the same parameterization introduced in section II (Eqns. (33) and (48)) for the single-field case, which specifies the amplitude, location, duration, and wavelength band over which each event is effective.

In Figure 9, we show the evolution of the Wigner ellipse

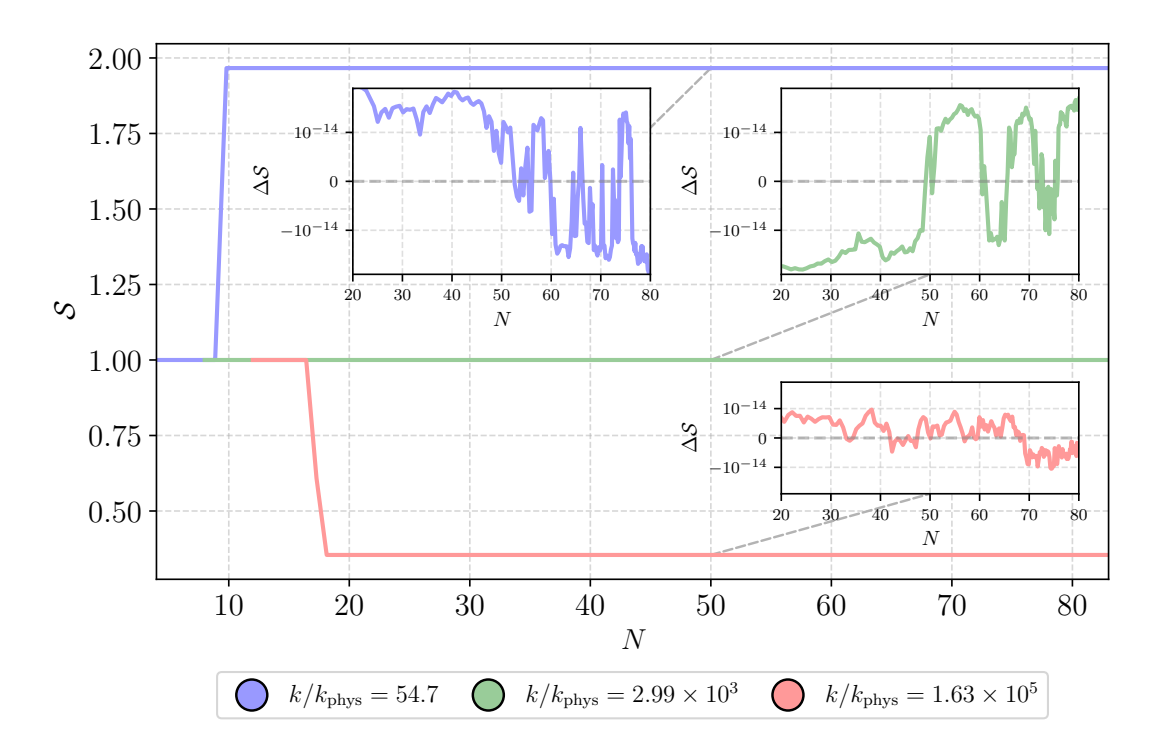


FIG. 10. Evolution of the determinant for the modes considered in Figure 9. As expected, changes in the determinant only occur while the decoherence events are active. The insets depict the deviation of the determinant from its mean value, computed from the period following the decoherence event up to the end of inflation. These deviations confirm that the conservation of S is preserved to machine precision, and also that errors do not propagate after traversing the state-deformation tiles.

as it undergoes decoherence and recoherence events of finite duration. As illustrated in the left panel of this figure, we considered three modes with different wavenumbers kin order to compare the ellipse evolution in three cases: with a single decoherence event (in blue, passing through a brown rectangle), no events (in green) and with a single recoherence event (in red, crossing a yellow rectangle). Although some mild dephasing naturally occurs even in the absence of decoherence – since modes with different k cross the horizon at different times – the effects of decoherence and recoherence events dominate the evolution. These events produce noticeable changes in the area of the Wigner ellipse, which in turn make the resulting squeezing and additional dephasing visually evident. Therefore, our approach of using different k-modes remains an efficient way to illustrate and contrast the deformations induced by such "accidents" with those in the environment-free scenario. To setup the decoherence events, we consider the tile parameterization in Eq. (33): the decoherence accident has $\alpha_{\Gamma} = 0.35$ and p = 3. It is centered at $(N, \ln \ell) = (10.0, 9.0)$, has a height of $\Delta \ell = 0.4$ and a width of $\Delta N = 4$. The recoherence event has $\alpha_{\Gamma} = -0.35$, is located at $(N, \ln \ell) = (16.0, 9.0)$ and has the same width, height and value of p as the area-increasing accident. The shape of the horizon corresponds to the two-field nonlinear potential presented at the beginning of this section in Eq. (51), producing almost 84 e-folds of inflation.

In the right panel of Figure 9, we show the projections

of the Wigner ellipse at a fixed instant of time for the same modes displayed in the left panel. As a representative example, we consider the case where both fields contribute equally to the interaction operator

$$\hat{I}_{\mathbf{k}}^{\mathbf{S}} = \hat{v}_{\mathbf{S}}^{\phi} + \hat{v}_{\mathbf{S}}^{\sigma} , \qquad (101)$$

where this choice sets $\alpha_{\phi}=\alpha_{\sigma}=1,\ \beta_{\phi}=\beta_{\sigma}=0,$ while the labels ϕ and σ refer to the ϕ and σ background field components of the nonlinear potential. Together with the tile parameters, this specifies all of the source term components \mathcal{F}_{AB} entering the dynamical coloring transformations defined by Eqns. (90), (95), and (96). Furthermore, from this panel, it is clear that the area of the ellipse is increased by the decoherence event, while the recoherence event reduces it. It is also evident that these events not only affect the area, but also the squeezing and the rotation phases, depicted by the orthogonal dashed lines in each projection. Variations in the area are further confirmed by the marginalized distributions $\rho_k(v_S^A)$ and $\rho_k(\pi_S^A)$, which broaden as the modes cross a decoherence tile with $\alpha_{\Gamma} > 0$ and narrow when traversing a tile with $\alpha_{\Gamma} < 0$. Although not shown here, as a consistency check, we compared the power spectrum produced by a separate code solving numerical mode evolution with our Cholesky decomposition transport scheme in the decoherence-free case for the nonlinear potential, obtaining the same results. We will present an alternative fast and slow scale separation approach based in the evolution of the mode

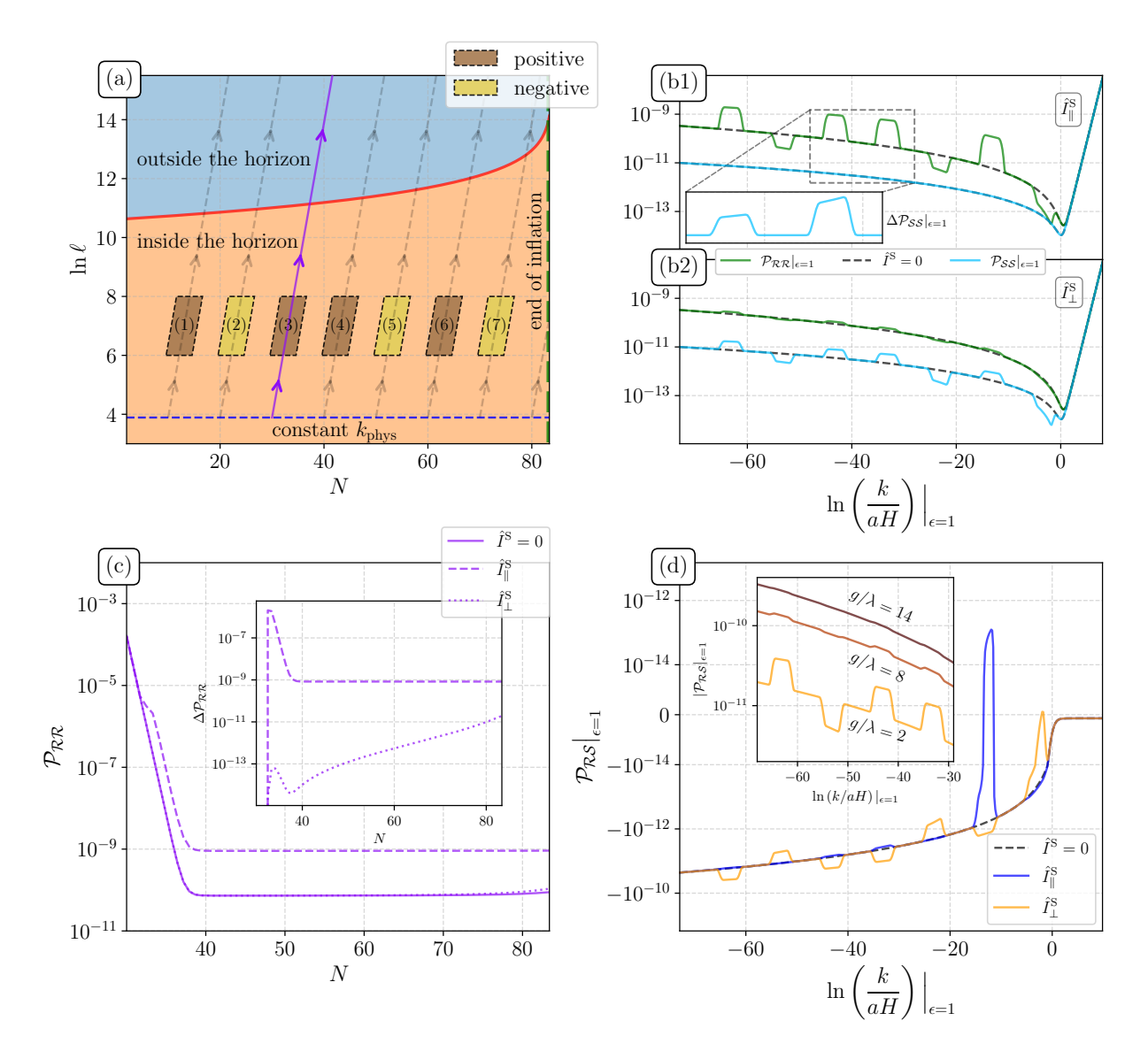


FIG. 11. Mode correlators resulting from the implementation of the two decoherence channels built from the environmental operators \hat{I}_{\parallel}^{S} and \hat{I}_{\perp}^{S} defined in Eqns. (102a–102b). Panel (a): Mode-injection scheme with an array of decoherence events, using the same tiling in the $(N, \ln \ell)$ plane for both operators. The highlighted mode (purple dashed line) shows the evolution of mode correlators across each decoherence region. Panels (b1) and (b2): Parallel ($\mathcal{P}_{\mathcal{R}\mathcal{R}}$) and perpendicular ($\mathcal{P}_{\mathcal{S}\mathcal{S}}$) spectra for the \hat{I}_{\parallel}^{S} and \hat{I}_{\perp}^{S} operators. Each operator imprints features primarily on its corresponding spectrum, with residual structures in $\mathcal{P}_{\mathcal{R}\mathcal{R}}$ arising from small correlations between isocurvature and adiabatic modes. Panel (c): Evolution of the $\mathcal{P}_{\mathcal{R}\mathcal{R}}$ k-mode highlighted in Panel (a), as it crosses parallel and perpendicular decoherence events. The inset shows the variation $\Delta \mathcal{P}_{\mathcal{R}\mathcal{R}}$ relative to the accident-free scenario ($\hat{I}^{S}=0$), indicating that $\mathcal{P}_{\mathcal{R}\mathcal{R}}$ modes grow when crossing the \hat{I}_{\perp}^{S} configuration, which is consistent with the presence of the small-amplitude features visible (in green) in panel (b2). Panel (d): Cross correlators ($\mathcal{P}_{\mathcal{R}\mathcal{S}}$) for the same setup. The large spike (in blue) marks a sign flip rather than a change in correlation magnitude. The inset illustrates how increasing the field coupling enhances the amplitude of cross correlations. Features are present in all of the cases.

equations in a future project.

An animation accompanying our results in Figure 9, provided as an ancillary file, illustrates the full evolution of the joint Wigner function as the modes traverse decoherence/recoherence events for the same tile parameters considered in this figure. In this animation, the evolution also includes the deformation of the ellipse during horizon crossing. A second animation shows the generation of

squeezed states under a different sequence of tiles for the single-field version of this model (i.e., $V(\phi) = \lambda \phi^4/4$).

As in the single-field case, the evolution of the covariance matrix determinant \mathcal{S} provides a diagnostic of the possible instabilities emerging during the dynamical coloring evolution. In Figure 10, we show the evolution of \mathcal{S} for the same three modes displayed in Figure 9, corresponding respectively to cases where the area of the Wigner ellipse

increases, decreases, and remains unchanged during the decoherence events. Similar to panel (d) in Figures 4 and 5 for the case of one field, variations in the determinant only occur while decoherence events are active. To test whether numerical errors accumulate over time, we computed the deviation ΔS between the instantaneous value of the determinant and its mean value over the interval $N \in [20, 83.5]$. The lower bound of this interval corresponds to an arbitrary instant of time sufficiently close to the onset of decoherence (or recoherence) events. The insets of Figure 10 show that the deviation remain at the level of double precision round-off errors, confirming the stability of the numerical evolution scheme. The code publicly available in this paper uses an A-stable eighth-order symplectic Gauss-Legendre integrator [44] to numerically resolve the time evolution of the mode correlators.

The interaction operator parameterization introduced in Eq. (79) suggests that the isentropic and the isocurvature components can be treated as distinct channels through which decoherence effects may manifest. For simplicity, the two-field realization considered in this section only requires interaction operators of the form

$$\hat{I}_{\parallel}^{S} = \alpha_{\parallel}^{\phi}(\tau)\hat{v}_{\parallel}^{\phi} + \alpha_{\parallel}^{\sigma}(\tau)\hat{v}_{\parallel}^{\sigma}, \qquad (102a)$$

$$\hat{I}_{\perp}^{S} = \alpha_{\perp}^{\phi}(\tau)\hat{v}_{\perp}^{\phi} + \alpha_{\perp}^{\sigma}(\tau)\hat{v}_{\perp}^{\sigma}, \qquad (102b)$$

which follow directly from the field definitions along the parallel and perpendicular directions in Eqns. (78a–78b), respectively. To treat separately the decoherence effects associated with the parallel $\left\langle \left\{ \hat{v}_{\perp}^{A}, \hat{v}_{\parallel}^{A} \right\} \right\rangle$ and perpendicular $\left\langle \left\{ \hat{v}_{\perp}^{A}, \hat{v}_{\perp}^{A} \right\} \right\rangle$ contributions of the power spectrum, it is sufficient to assign time-independent values to the coefficients α_{\parallel} and α_{\perp} . Thus, for simplicity, we fix all the components of α_{\parallel} and α_{\perp} to one. For compactness in the notation, we define the following normalized correlators with respect to these contributions:

$$N_v \equiv \frac{k^3}{4\pi^2} \left[\frac{H}{a||\dot{\phi}||^2} \right]^2 \quad , \quad \mathcal{P}_{\mathcal{R}\mathcal{R}} \equiv N_v \left\langle \{\hat{v}_{\parallel}^A, \hat{v}_{\parallel}^A\} \right\rangle \,, \tag{103a}$$

$$\mathcal{P}_{\mathcal{RS}} \equiv N_v \left\langle \{ \hat{v}_{\parallel}^A, \hat{v}_{\perp}^A \} \right\rangle \quad , \quad \mathcal{P}_{\mathcal{SS}} \equiv N_v \left\langle \{ \hat{v}_{\perp}^A, \hat{v}_{\perp}^A \} \right\rangle$$
(103b)

where, apart from the normalization factor, this notation is consistent with previous work (i.e., [45-47] and others).

Considering the interaction operator definitions introduced above, our results in Figure 11 display the power, cross-correlations and the dynamical effects from decoherence events in the evolution of the mode correlators defined in Eqns. (103a-103b) for arbitrary values of k. These results are obtained by configuring a fixed sequence of decoherence events sourced separately by the parallel and perpendicular operators. Individual tiles are built following the parallelogram parameterization introduced in Eq. (48).

Event	α_{Γ}		$\ln\left(\frac{k_j}{k_j}\right)$
	$\hat{I}_{\parallel}^{ m S}$	$\hat{I}_{\perp}^{ m S}$	$\frac{111}{k_{\text{phys}}}$
(1)	0.25	0.46	10.0
(2)	-0.075	-0.280	20.0
(3)	0.25	0.37	30.0
(4)	0.25	0.34	40.0
(5)	-0.058	-0.2	50.0
(6)	0.25	0.2	60.0
(7)	-0.04	-0.1	70.0

TABLE I. Tile parameters for the configuration of decoherence events sourced by parallel $(\hat{I}_{\perp}^{\rm S})$ and perpendicular $(\hat{I}_{\perp}^{\rm S})$ operators in Figure 11, panel (a). The remaining tile parameters (i.e., the widths, vertical locations along the $\ln \ell$ axis and heights) are constant.

In Figure 11, panel (a), we present the mode-injection scheme based on the same two-field nonlinear potential used throughout this section $V(\phi, \sigma) = \lambda \phi^4/4 + g\phi^2\sigma^2/2$ with $\lambda = 10^{-14}$ and $g = 2\lambda$. The background initial conditions were chosen to yield approximately 83 e-folds of inflation. In this setup, both the parallel and perpendicular operators source the same distribution of decoherence events, arranged as a single sequence of tiles shown in panel (a). We report some of the main properties of each tile in Table I. From this scheme, it can be seen that the following features in the $(N, \ln \ell)$ space are common to all tiles: the position along the vertical axis, the height in the length scale and the width along the injection scale are fixed with $\ln \ell_j = 7$, $\Delta \ell_{ij} = 2$ and $\sinh^{-1}(\Delta k_{ij}/2k_i) = 5$.

In Figure 11, panels (b1) and (b2) show the evolution of the isocurvature (\mathcal{P}_{SS}) and isentropic (\mathcal{P}_{RR}) power spectra as the mode correlators pass through the same sequence of decoherence events depicted in panel (a). Panel (b1) corresponds to decoherence events driven by the environmental operator $\hat{I}^{\mathrm{S}}_{\parallel}$. At first glance, spectral deformations appear only in the isentropic spectrum $\mathcal{P}_{\mathcal{R}\mathcal{R}}$. However, a more careful evaluation of the differences with respect to the accident-free scenario reveals faint imprints in the isocurvature spectrum \mathcal{P}_{SS} . As highlighted in the inset at the lower-left corner, which displays the difference in adiabatic mode power $(\Delta \mathcal{P}_{SS})$ with respect to the case free of environmental effects, these residual structures follow the shape of the decoherence tiles but have almost negligible amplitudes. Panel (b2) presents the analogous effects induced by the perpendicular operator I_{\perp}^{S} . In contrast to panel (b1), the isocurvature power spectrum (\mathcal{P}_{SS}) now exhibits visible intermittent deviations, while the isentropic spectrum remains approximately featureless. The results in both panels clearly indicate the presence of weak cross-correlations between entropy and curvature modes, allowing the propagation of decoherence events active in one direction to propagate to the other. Furthermore, the combined configuration of parallel and perpendicular environmental operators resembles the action of a beam-splitter, where the adiabatic and isocurvature modes play an role analogous to orthogonal polarization states in a quantum optics setup. The

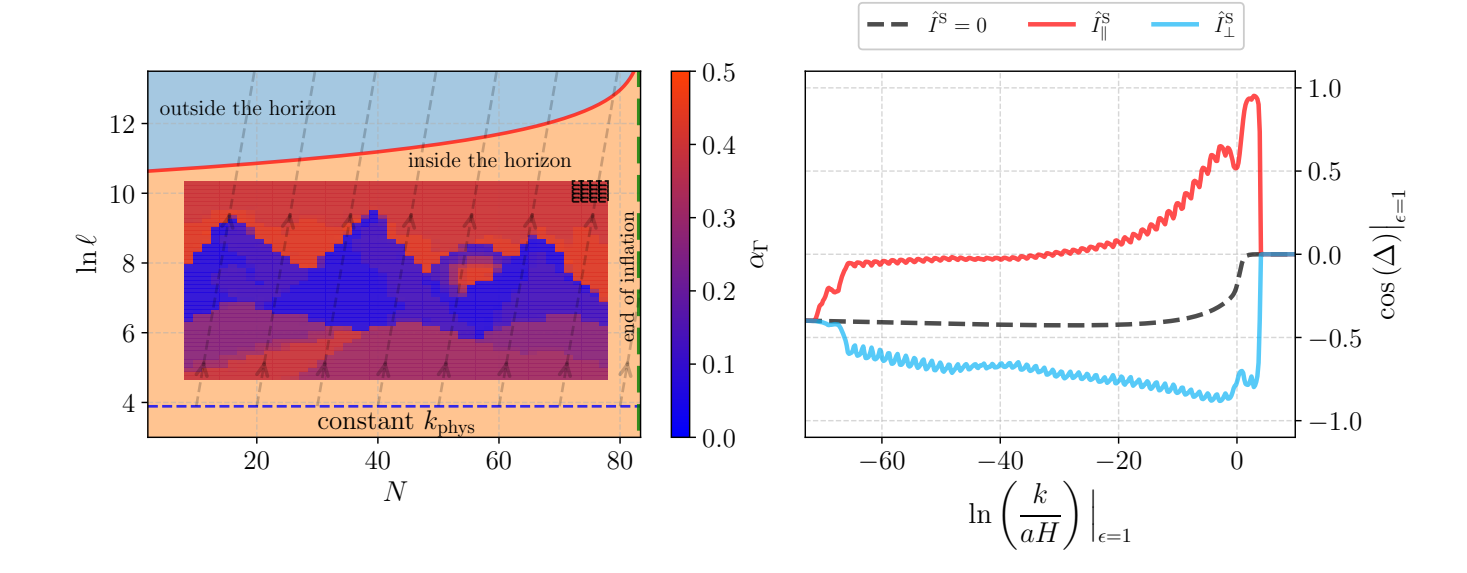


FIG. 12. Deformations in the mode cross-correlations for a large number of decoherence tiles generated by parallel and perpendicular environmental operators. Left panel: mode injection scheme with a 48 × 48 array of decoherence events (with $\alpha_{\Gamma} > 0$) forming a landscape pattern. The small 5 × 4 array in the upper right corner shows the duration and the k-span for each accident in real magnitude. As in the single-field scenario depicted in Figure 6, the code resolves the dynamics of 365 modes within a few minutes, without showing signs of numerical instabilities. Right panel: resulting normalized mode cross-correlations, $\cos(\Delta)$, at the end of inflation in the cases $\hat{I}^{\rm S} = 0$, $\hat{I}^{\rm S}_{\parallel}$ and $\hat{I}^{\rm S}_{\perp}$ using the same tile pattern displayed in the left panel. Apart from the presence of features, it is evident that the choice of parallel/perpendicular operators flips the signs of the cross-correlations. The sharp decrease in $\cos(\Delta)$ at $k \gtrsim aH$ originates from a region free of events in the $(N, \ln \ell)$ plane. Wider arrays of tiles, incorporating mixed contributions from parallel and perpendicular operators, will enhance the cross-correlation power over that wavelength range.

action of this approximate beam-splitter can be further refined by tuning the parameters α_{\perp} and α_{\parallel} to minimize cross-correlation effects, a possibility that will be explored in a future project.

In Figure 11, panel (c), we show the evolution of the constant-k $\mathcal{P}_{\mathcal{R}\mathcal{R}}$ mode correlator as it undergoes decoherence events driven by either the parallel or perpendicular environmental operators. The trajectory corresponds to the mode depicted by the solid purple line in panel (a) of the same figure. To visualize the dynamical impact of each decoherence tile, we also display the corresponding evolution in the absence of environmental coupling $(\hat{I}^{S}=0)$. The evolution inside the horizon (before N=40) further illustrates the dynamical coloring transformations effectively implement a fast and slow scale separation scheme: as in the single-field case, none of the correlators computed involves algebraic phase cancellations through complex conjugation, since all quantities are real. Consequently, the plotted variables evolve slowly. This panel also confirms the expected behavior of the environmental operators: the parallel operator is more effective at deforming the dynamics of the curvature mode correlators. Although not shown here, an analogous result indicates that the perpendicular operator produces a similar effect on the entropy mode correlator. The inset within this panel shows the evolution of the differences with respect to

the accident-free case, illustrating that – even though the curvature mode correlator affected by the perpendicular operator remains several orders of magnitude smaller than in the case of the parallel decoherence event – the modes crossing the tiles sourced by $\hat{I}_{\perp}^{\rm S}$ still exhibit a monotonic growth over time after crossing the horizon. This growth is consistent with the emergence of small structures observed in Figure 11, panel (b2) in the isentropic power spectrum. If the correlation modes are allowed to evolve for longer times outside the horizon, this growth may lead to features of larger amplitude.

The results obtained in panels (b1), (b2) and (c) consistently emphasize the relevance of cross-correlations. To explore this further, we plot in Figure 11, panel (d), the entropy-curvature mode cross-correlators ($\mathcal{P}_{\mathcal{RS}}$) for the three configurations of tiles sourced by environmental operators. As in all of the previous cases, the cross-correlators retain the characteristic shape of the decoherence tiles that generate them, providing an additional check of the correct implementation of the dynamical system and a means to detect possible instabilities. In the high frequency regime, the tile patterns become convoluted with rapidly oscillating structures, which makes the underlying tile configuration harder to discern solely from shape of the spectrum. As shown in the panel, cross-correlator modes are allowed to be negative as long as the

full covariance matrix remains positive-definite. Moreover, the large blue spike demonstrates that decoherence events may be used to flip the signs of the correlations, thereby (in principle) altering the direction of power transfer between fields.

From the form of the two-field potential in Eq. (51), it follows that g is one of the parameters tuning the coupling between the background. Taking this into account, the inset of panel (d) shows that the magnitude of the entropy-curvature cross-correlations increases with the ratio g/λ . For this comparison, we adjusted the background field parameters so that each case (i.e., $g/\lambda = 2$, 8 and 14) produces the same number of e-folds of inflation. In all three cases, the constant k_{phys} hypersurface is fixed, inducing small shifts in the position of the horizon. As g increases, the horizon approaches the horizontal line denoting constant $k_{\rm phys}$, reducing the time of flight of the mode correlators inside the horizon and amplifying their magnitude. A closer inspection of the inset reveals that the characteristic features in the cross-correlations persist in every case, indicating that (a) the model parameters modulate the magnitude of the cross-correlators, and (b) features in the mode correlators can propagate between fields through their classical coupling. We observe that beyond mixing terms from the potential, the effective oscillation matrix Ω^2 in Eq. (60) also couples mode perturbations through background field time derivatives. This observation motivates the construction of numerical routines capable of incorporating the effects of sharp trajectories and propagating decoherence across different degrees of freedom. These aspects will be explored in a forthcoming project.

For sufficiently smooth evolution of the background trajectories, increasing the number of fields is not an obstacle to resolve a large amount of decoherence events generating state deformations during subhorizon evolution. We reuse the parallel and perpendicular operators defined in Eqns. (102a) and (102b) to construct an arrangement of 48×48 decoherence tiles in Figure 12. The left panel illustrates the mode injection scheme and displays a sequence of tiles that increase the area of the Wigner ellipse (i.e., with $\alpha_{\Gamma} \geq 0$), forming a landscape pattern in the $(N, \ln \ell)$ plane. Unlike the configuration used in Figure 11, panel (a), the tile parameterization here follows Eq. (33), which assumes rectangular rather than parallelogram tiles, as depicted in the small 5×4 array of events in the upper corner of this panel. In the right panel, we illustrate the impact of two distinct configurations of events - one sourced by the parallel environment operator $\hat{I}^{\mathrm{S}}_{\parallel}$ and the other by perpendicular ones $\hat{I}_{\perp}^{\rm S}$ – both built using the same tile layout depicted in the left panel. In contrast with the results shown in Figure 11, panel (d), here we represent cross-correlations using the variable

$$\cos(\Delta) \equiv \frac{\mathcal{P}_{\mathcal{RS}}}{\sqrt{\mathcal{P}_{\mathcal{RR}}\mathcal{P}_{\mathcal{SS}}}},$$
 (104)

which measures the relative strength of cross-correlations with respect to the amplitude of adiabatic and isocur-

vature spectra [45]. Our results demonstrate that decoherence events not only produce localized features in the spectra of mode correlators across different wavelength ranges, but also modifies both the direction and the magnitude of power transfer between fields.

IV. DISCUSSION

Decoherence, viewed in the framework of open-quantum systems, is itself a physically motivated phenomenon capable of inducing nontrivial state deformations [19– 21, 32, 34. Within this context, decoherence events may be interpreted as accidents that alter the course of state evolution – alterations that can be visualized as deformations of the Wigner ellipse representing the quantum state in phase space. However, given the flexibility of this framework, we adopt an alternative viewpoint: sequences of decoherence events can form a laboratory for driving primordial states toward specific dynamical configurations or target properties. One of such objectives is the generation of targeted features in the primordial curvature power spectrum, which are of phenomenological interest in nonlinear structure formation [26]. Although these features are usually associated with inflationary models that exhibit specific dynamical properties (e.g., [15, 30, 31, 40] and others), our implementation offers a computationally efficient way to reproduce such effects by modifying initial states. Moreover, within the context of single-field models, a natural next step – consistent with the framework of effective theory of inflation [38] – would be to propagate these modifications into the background expansion history, thereby introducing wavelength-dependent corrections (similar to our results in subsection IIC, Eq. (45)), and opening an interesting avenue for future research.

In this project, we present a numerical implementation that incorporates the simplest non-unitary decoherence corrections into the dynamics of inflationary fluctuations at the level of two-point correlators. These corrections enable controlled manipulations of the initial Gaussian states in a way analogous to a pumping protocol in quantum optics. The method accommodates arbitrary arrangements of decoherence events and accounts for nonlinear background field evolution without relying on the slow-roll approximations. Furthermore, this approach has been extended to evaluate systems with multiple fields that undergo coupling through the time-evolving background fields. The numerical implementation employs the Wigner representation of Gaussian states to perform dynamical coloring transformations – which, as demonstrated in [27], act as a fast-slow scale separation scheme that efficiently suppresses the highest oscillation scales of a problem.

Part of the flexibility of this alternative viewpoint comes from the possibility of introducing events with negative decay rates, $\Gamma \tilde{C}_E < 0$, which we refer to as recoherence events. While this may lead to controversial interpretations, including possible conflicts with the uncertainty principle, it also broadens the class of effective dynamical

processes that can be explored and improves the precision with which the initial states can be prepared. We present an example of this versatility in Figure 5, where we built accident/anti-accident pairs. Here the effects generated by an event are compensated by a subsequent event with the opposite sign in its decay rate. This type of configuration induces intermittent state deformations that leave the primordial spectrum unaffected. Nevertheless, at the nonperturbative level, these intermittent decoherence events together with nonlinear potential deformations can source higher-order statistical moments in the distribution, including primordial non-Gaussianities.

As discussed in [21], the open-quantum system formulation applied to inflationary cosmology does not impose restrictions in the number of fields involved. Therefore, it is also reasonable to consider initial-state deformations arising from the coupling of a multifield system to an environment. In subsection IIIB, we derived the gauge transformations in Eqns. (76a–76d), which enable different forms of couplings through environment operators constructed from either fields or their conjugate momenta. In particular, an alternative coupling emerges from the projection into isocurvature and adiabatic modes, which suggests the existence of more than one channel through which decoherence may manifest. Our findings in subsection IIID exhibit a regime in which the effects of decoherence can be approximately decoupled: while the adiabatic spectrum is only slightly affected, the isocurvature sector undergoes stronger deformations.

As shown in Appendix B, the output of this coloring scheme can be used to produce three-dimensional field realizations suitable as initial conditions for nonlinear simulations of reheating, such as those in [29]. This makes it computationally efficient to generate large ensembles of field realizations, each corresponding to a distinct sequence of decoherence events. For instance, when considering a potential that supports oscillon formation—such as the monodromy potential proposed in [48]—the framework can be used to identify families of decoherence tiles that optimize oscillon production. This idea will be explored in forthcoming work.

ACKNOWLEDGMENTS

The authors would like to thank Jonathan Braden for many fruitful conversations which motivated this project. We would also like to thank Andrei Frolov, Stefano Gonzales, Lorena Luján, Jorge Medina, Diego Suárez, Sashwat Tanay and Vincent Vennin for their technical and logistic support, feedback and many valuable discussions resulting in the first versions of this paper. Part of the computations were performed on the cloud computational resources provided by Oracle. The work of JP and JG was partially funded by Fondo Semilla 2023, granted by Universidad de Ingeniería y Tecnología. The work of GQ was funded in part by NSERC Discovery Grant "Testing fundamental physics with B-modes on Cosmic Microwave Background

anisotropy". This project was funded by CONCYTEC through the PROCIENCIA program in the context of the research opportunity "E041-2024-03. Proyectos de Investigación Básica", contract number PE501087705-2024-PROCIENCIA.

Appendix A: Other factorization schemes for dynamical coloring transformations

As discussed in subsection III C, the two-point correlation function $\langle \hat{v}_A, \hat{v}_B \rangle$ defines a symmetric and positive-definite matrix and therefore admits a factorization of the form

$$\langle \hat{v}_A^{\mathrm{S}}, \hat{v}_B^{\mathrm{S}} \rangle = L_{AC} L_{CB}^{\mathrm{T}}, \tag{A1}$$

where ${\bf L}$ is a real matrix. In constructing dynamical coloring transformations based on Cholesky decomposition, we fixed the shape of the factors to be triangular. However, as noted previously, this choice is not unique. In this appendix, we examine an alternative scheme in which ${\bf L}$ is taken to be symmetric rather than triangular, noting that both decompositions involve the same number of degrees of freedom.

To this end, we revisit the derivation of the coloring transformations, beginning with the redefinition of the purely real (or imaginary) field multiplet and its conjugate momenta

$$\hat{v}_{S}^{A} \to L_{AB} \tilde{\chi}_{B} \,, \tag{A2}$$

$$\hat{\pi}_{S}^{A} \to L'_{AB}\tilde{\chi}_{B} + L_{AB}\tilde{\chi}'_{B},$$
 (A3)

here the matrix ${\bf L}$ encodes the amplitude correlations among field components, and $\tilde{\chi}$ denotes a vector of Gaussian random variables spanning the relevant region of phase space. These random variables are normalized such that their two-point correlator satisfies

$$\langle \tilde{\chi}_A, \tilde{\chi}_B \rangle = \delta_{AB} \,. \tag{A4}$$

Differentiating Eq. (A4) twice with respect to conformal time yields the following consistency relations:

$$\operatorname{Sym}_{AB}^{CD} \left[\langle \tilde{\chi}'_C, \tilde{\chi}_D \rangle \right] = 0,$$

$$\operatorname{Sym}_{AB}^{CD} \left[\langle \tilde{\chi}''_C, \tilde{\chi}_D \rangle + \langle \tilde{\chi}'_C, \tilde{\chi}'_D \rangle \right] = 0,$$
(A5)

where the symmetrization operator is defined as Sym $X \equiv X + X^{T}$. Substituting these relations in the covariance matrix definitions in Eqns. (80a–80c), and then into the transport equations in Eqns. (75a–75c), we obtain the following condition for the coloring factors

$$\operatorname{Sym}_{AB}^{CD} \left[(L^{-1})_{CE} L_{ED}^{"} - \mathcal{Z}_{CD} + (L^{-1})_{CE} \Omega_{EF}^{2} L_{FD} + 2(L^{-1})_{CE} L_{EF}^{'} \langle \tilde{\chi}_{F}^{'}, \tilde{\chi}_{D} \rangle + \langle \tilde{\chi}_{C}^{'}, \tilde{\chi}_{E} \rangle \langle \tilde{\chi}_{E}^{'}, \tilde{\chi}_{D} \rangle \right] = 0,$$
(A6)

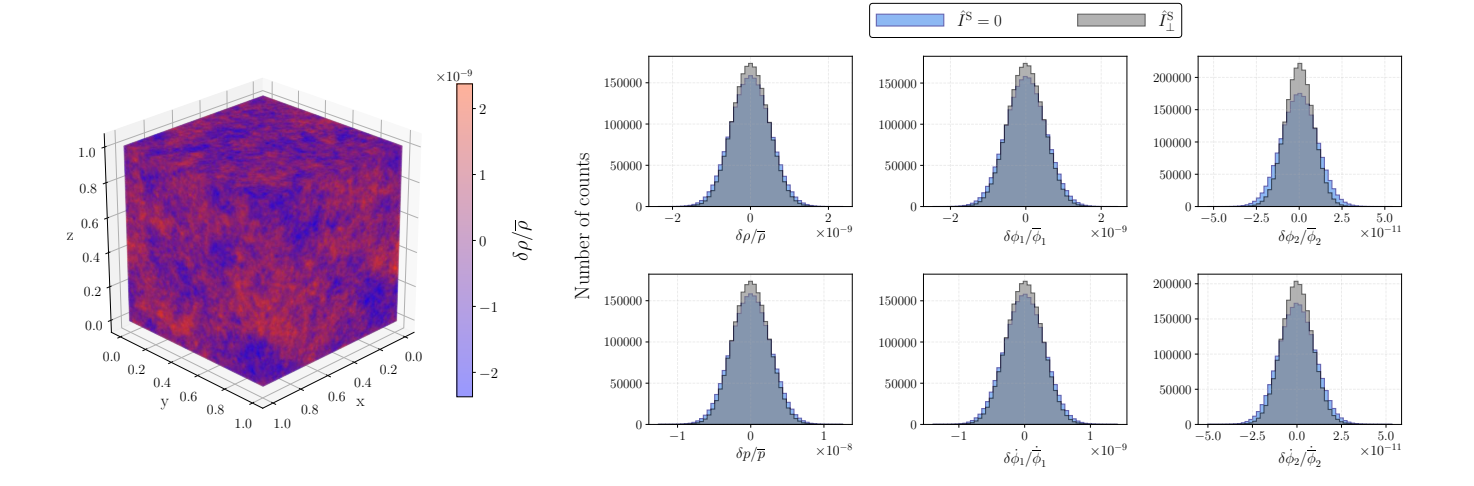


FIG. 13. Three-dimensional realization of the field and energy density fluctuations at the end of inflation obtained through dynamical coloring transformations. Left panel: spatial distribution of energy density fluctuations in a 128^3 box, computed with the nonlinear potential in Eq. (51) and Fourier-based spatial derivatives for the gradient energy. Right panel: histograms of the field, momentum, density and pressure fluctuations after the system crosses an array of decoherence tiles generated by perpendicular environmental operators \hat{I}_{\perp}^{S} . The resulting Gaussian distributions remain close to their decoherence-free counterparts, indicating that decoherence acting on isocurvature modes does not necessarily induce large changes in the initial conditions for reheating.

where $\mathcal{Z} \equiv \langle \tilde{\chi}', \tilde{\chi}' \rangle + \langle \tilde{\chi}', \tilde{\chi} \rangle \langle \tilde{\chi}', \tilde{\chi} \rangle$ is the only other variable, aside from the decomposition matrices, that appears in the determinant of the covariance matrix. The overall

symmetrization allows the inclusion of an antisymmetric matrix \mathcal{A} that fixes the shape of the L, leading to the equations of motion

$$L_{AB}'' + \Omega_{AC}^2 L_{CB} + 2L_{AC}' \langle \tilde{\chi}_C', \tilde{\chi}_B \rangle - L_{AC} \left[\mathcal{Z}_{CB} - \langle \tilde{\chi}_C', \tilde{\chi}_D \rangle \langle \tilde{\chi}_D', \tilde{\chi}_B \rangle \right] + L_{AC} \mathcal{A}_{CB} = 0, \tag{A7}$$

which is the only instance where the form of \boldsymbol{L} can change. As in the Cholesky-based decomposition scheme, fixing the shape of the matrix requires to identify the shapes of each term in the equations of motion. For convenience, we define

$$P_{AB} \equiv \Omega_{AC}^{2} L_{CB} + 2L_{AC}' \langle \tilde{\chi}_{C}', \tilde{\chi}_{B} \rangle - L_{AC} \left[\mathcal{Z}_{CB} - \langle \tilde{\chi}_{C}', \tilde{\chi}_{D} \rangle \langle \tilde{\chi}_{D}', \tilde{\chi}_{B} \rangle \right]. \tag{A8}$$

From Eq. (A7), \boldsymbol{L} remains symmetric at all times if and only if the combination $\boldsymbol{P} + \boldsymbol{L}\boldsymbol{\mathcal{A}}$ is symmetric, which implies

$$\mathbf{P} + \mathbf{L} \mathbf{\mathcal{A}} = \mathbf{P}^{\mathrm{T}} - \mathbf{\mathcal{A}} \mathbf{L} \,, \tag{A9}$$

rearranging terms in this expression, we find that ${\cal A}$ satisfies the Sylvester equation

$$\{\mathbf{L}, \mathbf{A}\} = \mathbf{Q}, \tag{A10}$$

where $\{\cdot,\cdot\}$ is the anticommutator and

$$\mathbf{Q} \equiv \mathbf{P}^{\mathrm{T}} - \mathbf{P} = -\operatorname{Antisym}[\mathbf{P}]. \tag{A11}$$

Since \boldsymbol{L} is symmetric, it can be diagonalized by an orthonormal matrix \boldsymbol{O} , such that

$$\mathbf{O}^{\mathrm{T}}\mathbf{LO} = \mathbf{L}^{\mathrm{D}}, \qquad (A12)$$

where L^{D} is diagonal. In this diagonal basis of L, the Sylvester equation becomes

$$\mathbf{L}^{\mathrm{D}} \mathbf{\mathcal{A}}^{\mathrm{D}} + \mathbf{\mathcal{A}}^{\mathrm{D}} \mathbf{L}^{\mathrm{D}} = \mathbf{Q}^{\mathrm{D}}, \qquad (A13)$$

with $\mathcal{A}^{D} = \mathbf{O}^{T} \mathbf{A} \mathbf{O}$. In component form (no summation over repeated indices), this reads

$$\sum_{J=1}^{\mathcal{N}} \left(L_A^{\mathcal{D}} \delta_{AJ} \mathcal{A}_{JB}^{\mathcal{D}} + \mathcal{A}_{AJ}^{\mathcal{D}} L_J^{\mathcal{D}} \delta_{JB} \right)$$

$$= L_A^{\mathcal{D}} \mathcal{A}_{AB}^{\mathcal{D}} + \mathcal{A}_{AB}^{\mathcal{D}} L_B^{\mathcal{D}} = Q_{AB}^{\mathcal{D}}, \qquad (A14)$$

which implies that the elements of \mathcal{A}^{D} are given by

$$\mathcal{A}_{AB}^{\rm D} = \frac{Q_{AB}^{\rm D}}{L_A^{\rm D} + L_B^{\rm D}} \,. \tag{A15}$$

Finally, \mathcal{A} can be reconstructed as

$$\mathbf{A} = \mathbf{O}\mathbf{A}^{\mathbf{D}}\mathbf{O}^{\mathbf{T}}.$$
 (A16)

Hence, with this construction of the antisymmetric matrix \mathcal{A} , it is possible to ensure that the factor L, which evolves according to Eq. (A7), will be symmetric at all times. The correlators involving derivatives of the random variables close the dynamical system, and their equations of motion – given in Eqns. (90) and (95) – remain unaltered. This example shows that it is possible to implement dynamical coloring transformations using other decomposition schemes. However, we are still not able to confirm that this procedure works effectively as a fast and slow separation scheme. A more detailed analysis of alternative decomposition schemes will be explored in a future project.

Appendix B: Building three-dimensional Gaussian field realizations

Apart from separating the fast and slow oscillation scales – which already provides a computational advantage – the dynamical coloring scheme also produces output in a format suitable directly compatible with nonlinear codes used to evolve fields during reheating (e.g., [29]). In these evolution routines, the first step is to generate spatial realizations of the fields and their derivatives that serve as initial conditions. To construct them, we must compute the mode correlators of the original field-perturbation variables in cosmic time

$$\langle \Phi_{\mathbf{k}}^A, \Phi_{\mathbf{k}}^B \rangle = \frac{1}{a^2} L^{AC} (L^{\mathrm{T}})^{CB} , \qquad (B1)$$

$$\langle \Phi_{\mathbf{k}}^{A}, \dot{\Phi}_{\mathbf{k}}^{B} \rangle = \frac{1}{a^{3}} L'^{AC} (L^{T})^{CB} - \frac{H}{a^{2}} L^{AC} (L^{T})^{CB} + \frac{1}{a^{3}} L^{AC} \langle \tilde{\chi}'^{C}, \tilde{\chi}^{E} \rangle (L^{T})^{EB},$$
 (B2)

$$\langle \dot{\Phi}_{\mathbf{k}}^{A}, \dot{\Phi}_{\mathbf{k}}^{B} \rangle = \frac{1}{a^{4}} \bigg\{ L'^{AC} (L'^{\mathrm{T}})^{CB} - L^{AC} \langle \tilde{\chi}'^{C}, \tilde{\chi}^{D} \rangle \langle \tilde{\chi}'^{D}, \tilde{\chi}^{E} \rangle (L'^{\mathrm{T}})^{EB} + L^{AC} \mathcal{Z}^{CD} (L'^{\mathrm{T}})^{DB} \\$$

$$-a^{2}H^{2}L^{AC}(L^{\mathrm{T}})^{CB} - \operatorname{Sym}_{CD}^{AB} \left[L^{\prime CE} \langle \tilde{\chi}^{\prime E}, \tilde{\chi}^{F} \rangle (L^{\mathrm{T}})^{FD} + aHL^{\prime CE}(L^{\mathrm{T}})^{ED} \right] \right\}, \tag{B3}$$

which are written with respect to the dynamical variables of the coloring scheme in conformal time at initial time $t=t_0$. Here we only considered the real part of the field operators (S = R), since for our choice of interaction operators – at the end of inflation – the imaginary part does not introduce more information. Together, the correlators in Eqns. (B1–B3) form a $2\mathcal{N} \times 2\mathcal{N}$ symmetric matrix

$$\Psi_{\mathbf{k}}(t_0) = \begin{bmatrix} \langle \Phi_{\mathbf{k}}^A, \Phi_{\mathbf{k}}^B \rangle & \langle \dot{\Phi}_{\mathbf{k}}^A, \Phi_{\mathbf{k}}^B \rangle \\ \langle \dot{\Phi}_{\mathbf{k}}^A, \Phi_{\mathbf{k}}^B \rangle & \langle \dot{\Phi}_{\mathbf{k}}^A, \dot{\Phi}_{\mathbf{k}}^B \rangle \end{bmatrix},$$
(B4)

which follows the reality condition $\Psi_{\mathbf{k}}^* = \Psi_{-\mathbf{k}}$. For adequate spectral resolution, we first interpolate the correlation matrix on a logarithmic scale and then transform it to real space using an inverse discrete Fourier transform $\Psi_r(t_0) \equiv \mathrm{DFT}^{-1}[\Psi_{\mathbf{k}}(t_0)]$.

Spatial realizations of the field and its derivative are constructed by computing the Cholesky factors of the real-space correlation matrix

$$\mathbf{\Psi}_r(t_0) = \mathbf{\Lambda}(t_0)\mathbf{\Lambda}^{\mathrm{T}}(t_0), \qquad (B5)$$

and multiplying the resulting factor by a $2\mathcal{N}$ -component vector of unit-variance random variables

$$V^m(t_0) = \Lambda^{mn}(t_0)\tilde{\chi}^n \,. \tag{B6}$$

Here $(m,n) \in [1,2\mathcal{N}]$, with the first \mathcal{N} components of $V(t_0)$ corresponding to the field and the remaining \mathcal{N} to its derivatives. In our implementation, each component of $\tilde{\chi}$ represents a vector of 128^3 spatial samples. These

provide a complete set of initial conditions for the \mathcal{N} fields that can be evolved in a reheating routine. We follow this approach to illustrate in Figure 13 the field, time-derivative, pressure and energy density fluctuations in three-dimensional space arising from our dynamical coloring transformation scheme at the end of inflation. We compute fluctuations in the energy density from

$$\rho(\mathbf{x}) = \frac{1}{2} \left[\dot{\phi}^A \dot{\phi}_A + \frac{1}{a^2} (\nabla^i \phi^A) (\nabla_i \phi_A) \right] + V(\phi, \sigma), \quad (B7)$$

considering the same two-field nonlinear potential (in Eq. (51)) used throughout the multifield section of this paper. We employ periodic boundary conditions to construct the gradient operator in Fourier domain and compute their energy contributions. Fluctuations are computed with respect to the average values over the entire box. In the left panel, we illustrate spatial fluctuations in the energy density in a 128^3 box, which are consistent with a normal distribution.

As shown in the right panel of Figure 13, the histograms of the field, momentum, energy-density, and pressure fluctuations remain consistent with Gaussian statistics, as anticipated from the premise established earlier in this appendix. To perform a preliminary test of decoherence, we compare two cases: one where the mode correlators traverse a layout of decoherence tiles sourced by the perpendicular operator $\hat{I}_{\perp}^{\rm S}$, and another without decoherence. The resulting distributions show only minor differences, in line with our results in subsection III D, Figure 11, panel

(b2), indicating regimes in which the perpendicular environmental operator exerts limited influence. This suggests

that decoherence through the isocurvature channel can be included without necessarily introducing significant distortions in the primordial curvature spectrum.

- A. H. Guth, The Inflationary Universe: A Possible Solution to the Horizon and Flatness Problems, Phys. Rev. D 23, 347 (1981).
- [2] J. M. Bardeen, P. J. Steinhardt, and M. S. Turner, Spontaneous Creation of Almost Scale Free Density Perturbations in an Inflationary Universe, Phys. Rev. D 28, 679 (1983).
- [3] V. F. Mukhanov, H. A. Feldman, and R. H. Brandenberger, Theory of cosmological perturbations. Part 1. Classical perturbations. Part 2. Quantum theory of perturbations. Part 3. Extensions, Phys. Rept. 215, 203 (1992).
- [4] A. A. Starobinsky, Spectrum of adiabatic perturbations in the universe when there are singularities in the inflation potential, JETP Lett. **55**, 489 (1992).
- [5] G. F. Smoot, COBE observations and results, AIP Conf. Proc. 476, 1 (1999), arXiv:astro-ph/9902027.
- [6] C. L. Bennett et al., Nine-Year Wilkinson Microwave Anisotropy Probe (WMAP) observations: final maps and results, The Astrophysical Journal Supplement Series 208, 20 (2013).
- [7] Y. Akrami et al. (Planck), Planck 2018 results. X. Constraints on inflation, Astron. Astrophys. 641, A10 (2020), arXiv:1807.06211 [astro-ph.CO].
- [8] P. Ade et al. (Simons Observatory), The Simons Observatory: Science goals and forecasts, JCAP 02, 056, arXiv:1808.07445 [astro-ph.CO].
- [9] K. Abazajian et al. (CMB-S4), CMB-S4: Forecasting Constraints on Primordial Gravitational Waves, Astrophys. J. 926, 54 (2022), arXiv:2008.12619 [astro-ph.CO].
- [10] S. Belkner, J. Carron, L. Legrand, C. Umiltà, C. Pryke, and C. Bischoff (CMB-S4), CMB-S4: Iterative Internal Delensing and r Constraints, Astrophys. J. 964, 148 (2024), arXiv:2310.06729 [astro-ph.CO].
- [11] E. Hertig, K. Wolz, T. Namikawa, A. Baleato Lizancos, S. Azzoni, and A. Challinor, The Simons Observatory: Combining delensing and foreground cleaning for improved constraints on inflation, in 58th Rencontres de Moriond on Cosmology (2024) arXiv:2405.13201 [astroph.CO].
- [12] R. Kallosh and A. Linde, Cosmological Attractors and Asymptotic Freedom of the Inflaton Field, JCAP 06, 047, arXiv:1604.00444 [hep-th].
- [13] R. Kallosh and A. Linde, On hilltop and brane inflation after Planck, JCAP 09, 030, arXiv:1906.02156 [hep-th].
- [14] R. Kallosh and A. Linde, Hybrid cosmological attractors, Phys. Rev. D 106, 023522 (2022), arXiv:2204.02425 [hep-th].
- [15] R. Kallosh, A. Linde, and D. Roest, Atacama Cosmology Telescope, South Pole Telescope, and Chaotic Inflation, Phys. Rev. Lett. 135, 161001 (2025), arXiv:2503.21030 [hep-th].
- [16] S. Renaux-Petel and K. Turzyński, Geometrical Destabilization of Inflation, Phys. Rev. Lett. 117, 141301 (2016), arXiv:1510.01281 [astro-ph.CO].
- [17] C. Armendariz-Picon, T. Damour, and V. F. Mukhanov, k - inflation, Phys. Lett. B 458, 209 (1999), arXiv:hep-

- th/9904075.
- [18] J. Martin and V. Vennin, Quantum discord of cosmic inflation: Can we show that cmb anisotropies are of quantummechanical origin?, Physical Review D 93, 10.1103/physrevd.93.023505 (2016).
- [19] J. Martin and V. Vennin, Non Gaussianities from Quantum Decoherence during Inflation, JCAP 06, 037, arXiv:1805.05609 [astro-ph.CO].
- [20] J. Martin and V. Vennin, Real-space entanglement in the Cosmic Microwave Background, JCAP 10, 036, arXiv:2106.15100 [gr-qc].
- [21] J. Martin, A. Micheli, and V. Vennin, Discord and decoherence, JCAP 04 (04), 051, arXiv:2112.05037 [quant-ph].
- [22] C. P. Burgess, R. Holman, G. Kaplanek, J. Martin, and V. Vennin, Minimal decoherence from inflation, JCAP 07, 022, arXiv:2211.11046 [hep-th].
- [23] D. Session *et al.*, Optical pumping of electronic quantum Hall states with vortex light, Nature Photon. **19**, 156 (2025), arXiv:2306.03417 [cond-mat.mes-hall].
- [24] I. Medina, S. R. Muniz, E. I. Goettems, and D. O. Soares-Pinto, Thermodynamics of the optical pumping process in Nitrogen-Vacancy centers, (2025), arXiv:2503.08769 [quant-ph].
- [25] J. R. Bond, L. Kofman, and D. Pogosyan, How filaments are woven into the cosmic web, Nature 380, 603 (1996), arXiv:astro-ph/9512141.
- [26] C. Stahl, D. Werth, and V. Poulin, Primordial sharp features through the nonlinear regime of structure formation, Phys. Rev. D 111, 123514 (2025), arXiv:2502.02571 [astro-ph.CO].
- [27] J. T. Gálvez Ghersi and A. V. Frolov, Two-point correlators revisited: Fast and slow scales in multifield models of inflation, JCAP 05, 047, arXiv:1609.04770 [astro-ph.CO].
- [28] J. T. Galvez Ghersi, A. Zucca, and A. V. Frolov, Observational Constraints on Constant Roll Inflation, JCAP 05, 030, arXiv:1808.01325 [astro-ph.CO].
- [29] A. V. Frolov, DEFROST: A New Code for Simulating Preheating after Inflation, JCAP 11, 009, arXiv:0809.4904 [hep-ph].
- [30] J. Martin, L. Sriramkumar, and D. K. Hazra, Sharp inflaton potentials and bi-spectra: Effects of smoothening the discontinuity, JCAP 09, 039, arXiv:1404.6093 [astroph.CO].
- [31] S. Bhattacharya and I. Zavala, Sharp turns in axion monodromy: primordial black holes and gravitational waves, JCAP 04, 065, arXiv:2205.06065 [astro-ph.CO].
- [32] J. Martin and V. Vennin, Quantum Discord of Cosmic Inflation: Can we Show that CMB Anisotropies are of Quantum-Mechanical Origin?, Phys. Rev. D 93, 023505 (2016), arXiv:1510.04038 [astro-ph.CO].
- [33] T. Colas, J. Grain, and V. Vennin, Four-mode squeezed states: two-field quantum systems and the symplectic group Sp(4, ℝ), Eur. Phys. J. C 82, 6 (2022), arXiv:2104.14942 [quant-ph].
- [34] J. Martin and V. Vennin, Observational constraints on quantum decoherence during inflation, JCAP **05**, 063,

- arXiv:1801.09949 [astro-ph.CO].
- [35] A. Bedroya and C. Vafa, Trans-Planckian Censorship and the Swampland, JHEP 09, 123, arXiv:1909.11063 [hep-th].
- [36] R. Brandenberger, Trans-Planckian Censorship Conjecture and Early Universe Cosmology, LHEP 2021, 198 (2021), arXiv:2102.09641 [hep-th].
- [37] M. Sasaki and E. D. Stewart, A General analytic formula for the spectral index of the density perturbations produced during inflation, Prog. Theor. Phys. 95, 71 (1996), arXiv:astro-ph/9507001.
- [38] S. A. Salcedo, T. Colas, and E. Pajer, The open effective field theory of inflation, JHEP 10, 248, arXiv:2404.15416 [hep-th].
- [39] S. Dimopoulos, S. Kachru, J. McGreevy, and J. G. Wacker, N-flation, JCAP 08, 003, arXiv:hep-th/0507205.
- [40] A. Achucarro, V. Atal, B. Hu, P. Ortiz, and J. Torrado, Inflation with moderately sharp features in the speed of sound: Generalized slow roll and in-in formalism for power spectrum and bispectrum, Phys. Rev. D 90, 023511 (2014), arXiv:1404.7522 [astro-ph.CO].
- [41] M. Konieczka, R. H. Ribeiro, and K. Turzynski, The effects of a fast-turning trajectory in multiple-field inflation,

- JCAP **07**, 030, arXiv:1401.6163 [astro-ph.CO].
- [42] D. Polarski and A. A. Starobinsky, Semiclassicality and decoherence of cosmological perturbations, Class. Quant. Grav. 13, 377 (1996), arXiv:gr-qc/9504030.
- [43] A. Kessy, A. Lewin, and K. Strimmer, Optimal whitening and decorrelation, The American Statistician 72, 309 (2018), https://doi.org/10.1080/00031305.2016.1277159.
- [44] J. C. Butcher, Implicit Runge-Kutta Processes, Mathematics of Computation 18, 50 (1964).
- [45] C. Gordon, D. Wands, B. A. Bassett, and R. Maartens, Adiabatic and entropy perturbations from inflation, Phys. Rev. D 63, 023506 (2000), arXiv:astro-ph/0009131.
- [46] C. T. Byrnes and D. Wands, Curvature and isocurvature perturbations from two-field inflation in a slow-roll expansion, Phys. Rev. D 74, 043529 (2006), arXiv:astro-ph/0605679.
- [47] Z. Lalak, D. Langlois, S. Pokorski, and K. Turzynski, Curvature and isocurvature perturbations in two-field inflation, JCAP 07, 014, arXiv:0704.0212 [hep-th].
- [48] M. A. Amin, R. Easther, H. Finkel, R. Flauger, and M. P. Hertzberg, Oscillons After Inflation, Phys. Rev. Lett. 108, 241302 (2012), arXiv:1106.3335 [astro-ph.CO].